



UNIVERSIDAD NACIONAL AUTÓNOMA DE MÉXICO

FACULTAD DE INGENIERÍA

**Interplay of slow-slip faults
beneath Mexico City induces
intense seismicity over
months**

ARTÍCULO ACADÉMICO

Que para obtener el título de

Ingeniera Geofísica

P R E S E N T A

Paulina Miranda García

ASESOR DE ARTÍCULO ACADÉMICO

Dr. Darío Emmanuel Solano Rojas



Ciudad Universitaria, Cd. Mx., 2025



**PROTESTA UNIVERSITARIA DE INTEGRIDAD Y
HONESTIDAD ACADÉMICA Y PROFESIONAL
(Titulación con trabajo escrito)**



De conformidad con lo dispuesto en los artículos 87, fracción V, del Estatuto General, 68, primer párrafo, del Reglamento General de Estudios Universitarios y 26, fracción I, y 35 del Reglamento General de Exámenes, me comprometo en todo tiempo a honrar a la institución y a cumplir con los principios establecidos en el Código de Ética de la Universidad Nacional Autónoma de México, especialmente con los de integridad y honestidad académica.

De acuerdo con lo anterior, manifiesto que el trabajo escrito titulado INTERPLAY OF SLOW-SLIP FAULTS BENEATH MEXICO CITY INDUCES INTENSE SEISMICITY OVER MONTHS que presenté para obtener el título de INGENIERO GEOFÍSICO es original, de mi autoría y lo realicé con el rigor metodológico exigido por mi Entidad Académica, citando las fuentes de ideas, textos, imágenes, gráficos u otro tipo de obras empleadas para su desarrollo.

En consecuencia, acepto que la falta de cumplimiento de las disposiciones reglamentarias y normativas de la Universidad, en particular las ya referidas en el Código de Ética, llevará a la nulidad de los actos de carácter académico administrativo del proceso de titulación.

PAULINA MIRANDA GARCIA
Número de cuenta: 316134682



Interplay of slow-slip faults beneath Mexico City induces intense seismicity over months

Manuel J. Aguilar-Velázquez^a, Paulina Miranda-García^a, Víctor M. Cruz-Atienza^b, Darío Solano-Rojas^{a,*}, Josué Tago^a, Luis A. Domínguez^b, Carlos Villafuerte^b, Víctor H. Espíndola^b, Delia Bello-Segura^c, Luis Quintanar-Robles^b, Mathieu Pertont^d

^a Facultad de Ingeniería, Universidad Nacional Autónoma de México, Mexico

^b Instituto de Geofísica, Universidad Nacional Autónoma de México, Mexico

^c Posgrado en Ciencias de la Tierra, Universidad Nacional Autónoma de México, Mexico

^d Instituto de Ingeniería, Universidad Nacional Autónoma de México, Mexico

ARTICLE INFO

Keywords:

Slow Slip events
Microseismicity
Interferometric SAR
Mexico City

ABSTRACT

In February 2023, a long seismic sequence began in western Mexico City causing widespread panic and some damage to housing infrastructure. On May 11 and December 14, two Mw3.2 mainshocks occurred at less than 700 m depth. Unprecedented satellite interferograms captured tectonic deformations in the two epicentral zones during the days surrounding the earthquakes. Data analysis revealed extended slip with maximum values around 8 cm on two sub-parallel east-west trending normal faults 800 m apart: namely the Barranca del Muerto (BM) fault to the south and the Mixcoac fault to the north. Detailed microseismicity analysis showed that 95 % of the slip on the BM fault was aseismic and initiated at least 6 days before the May 11 earthquake on the main asperity, located 1 km east of the hypocenter and ~ 1.2 km deep. For the December event on the Mixcoac fault, ~70 % of the slip was also aseismic but shallower (mostly above 600 m), which can be partially explained by the induced stresses on that fault due to the May slip on the BM fault. A quantitative geomorphological analysis allowed to establish the structural connection between both buried faults and their geomorphic expression to the west, with surface extensions of ~3.5 and ~ 4.5 km in the hilly area—where the most intense seismicity concentrates. The spatiotemporal patterns of fast and slow earthquakes suggest that the seismotectonics west of the city comprises two mechanically distinct zones: a stable region prone to aseismic deformation to the east where faults are buried under water-saturated sediments, and an unstable region to the west, prone to seismic radiation where faults are expressed geomorphologically. Thus, the seismic swarms in this area appear to result from the regional extensional regime, the stresses induced by slow slip on the eastern fault segments and interaction between these faults.

1. Introduction

It is well known that Mexico City, one of the world's most populated areas, is at great risk from earthquakes. Largely settled on ancient lake-bed sediments, the city experiences an amplification of seismic waves and a duration of strong motions that are among the largest known (Chávez-García and Bard, 1994; Cruz-Atienza et al., 2016; Ordaz and Singh, 1992; Reinoso and Ordaz, 1999; Singh et al., 1995). Subduction events such as the 1985 earthquake more than 300 km away (Singh et al., 1988), and intraslab ruptures like the 2017 earthquake 115 km south (Mirwald et al., 2019; Singh et al., 2018), have killed thousands of

people and severely damaged local infrastructure. Although these two types of events are the most common in Mexico, they are not the only ones threatening the country's capital. The Valley of Mexico is located in the Trans-Mexican Volcanic Belt (TMVB) where shallow crustal earthquakes with high intensities have occurred in the past. Two examples from the last century are the 1912 Acambay earthquake (Mw6.9) 80 km northwest of Mexico City, and the 1920 Xalapa earthquake (M ~ 6.4) 200 km to the east that killed at least 647 local people (Córdoba-Montiel et al., 2018; Flores and Camacho, 1922; Lacan et al., 2021; León-Loya et al., 2023; Urbina and Camacho, 1913). Pre-instrumental historical earthquakes have also been identified in the TMVB as having a

* Corresponding author.

E-mail address: dsolano@unam.mx (D. Solano-Rojas).

<https://doi.org/10.1016/j.tecto.2025.230659>

Received 5 July 2024; Received in revised form 11 December 2024; Accepted 10 February 2025

Available online 16 February 2025

0040-1951/© 2025 The Authors. Published by Elsevier B.V. This is an open access article under the CC BY license (<http://creativecommons.org/licenses/by/4.0/>).

significant hazard to society despite their large return periods (Bayona et al., 2017; Suárez et al., 2019, 2020).

Resulting from a transtensional stress regime, the faults that originate the TMVB crustal earthquakes have a preferential east-west and north-south orientation (Arce et al., 2019; Ferrari et al., 2012; Mooser, 1972; Suter et al., 1992). In the Valley of Mexico, which is in the south-central part of the TMVB (Fig. 1), although historically of small magnitude ($M < 4$), these earthquakes can be intense in the epicentral zone. Most occur in the foothills of the Sierra de las Cruces to the west of Mexico City (see Quintanar et al., 2024) and manifest as seismic swarm sequences (Figueroa, 1971; Manzanilla, 1986; Quintanar et al., 2024; Singh et al., 2020). Among the best studied are the 1981 swarm with an $M_L 3.3$ mainshock (Havskov, 1982) and the 2019 swarm whose $M_w 3.2$ mainshock produced the highest peak ground acceleration ever recorded on bedrock of the city (Singh et al., 2020) and panic among the

citizens (Fig. 1). In fact, this 2019 shock prompted the capital's authorities to unify the five seismic networks of the Valley of Mexico and its surroundings to create the Mexico City Seismic Network (MCSN), with more than 170 ultrasensitive (broadband) and strong motion seismic stations including borehole sites (Aguirre et al., 2021).

The underlying processes of local seismic swarms have been studied in different tectonic contexts. Swarm evolution is often thought to be governed by surrounding aseismic processes induced by fluid diffusion (Eyre et al., 2022). Transient aseismic fault slip in the form of shallow slow slip events can increase shear stress on the neighboring fault system and has been associated with seismic swarms along continental fault systems (Gualandi et al., 2017; Jiang et al., 2022; Lohman and McGuire, 2007; Siorattanakul et al., 2022). Besides, there is growing evidence that slow-slip phenomena are the driving process inducing intense seismicity where underground fluid diffusion is enhanced by injection

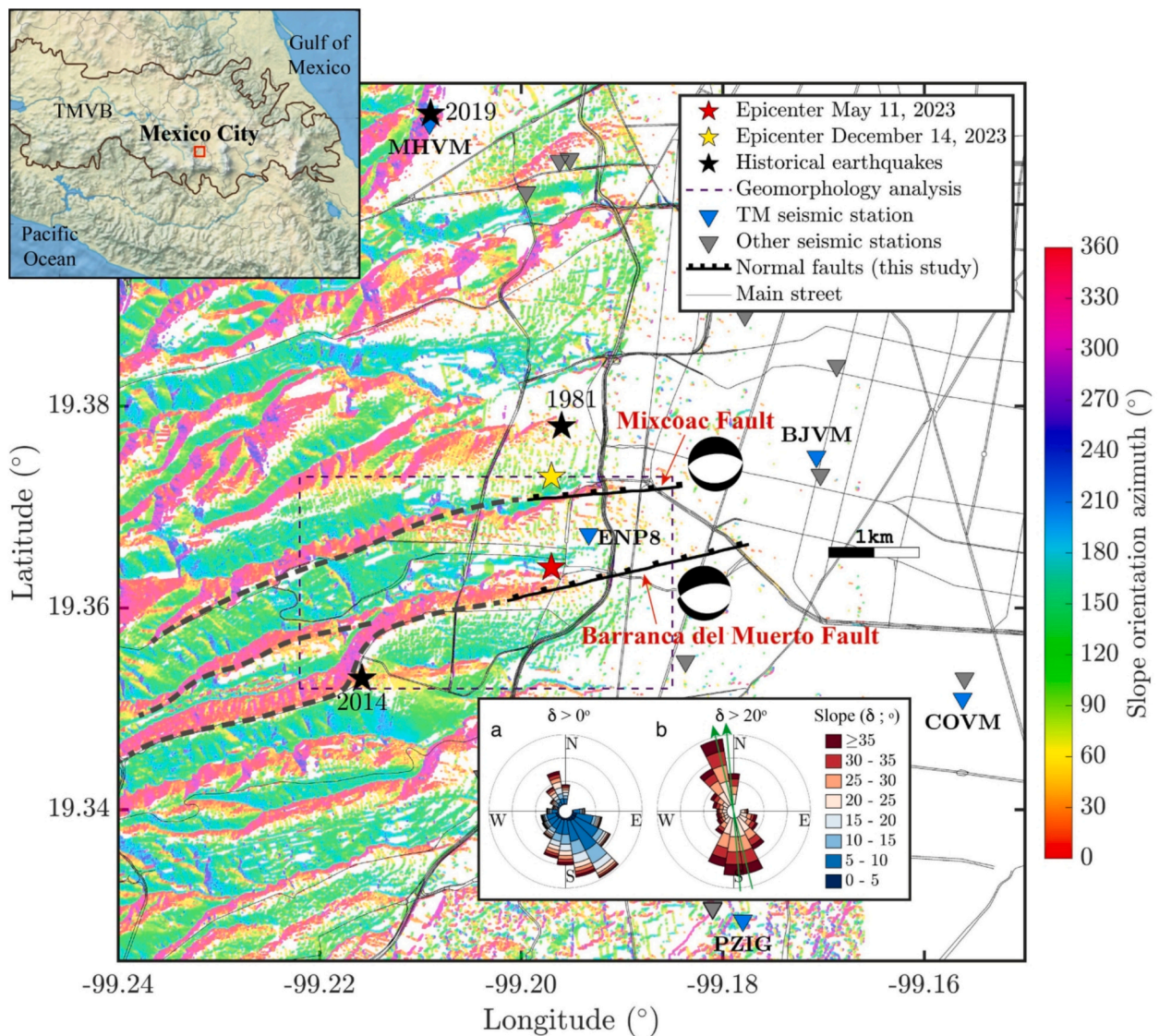


Fig. 1. Seismicity and Topographic Slope Orientation of the Study Area with the Barranca del Muerto (BM) and Mixcoac faults identified in this study. Upper left: Location map showing Mexico City in the south-central part of the Trans-Mexican Volcanic Belt (TMVB), Central Mexico. Main map: Orientation (aspect) of landscape slopes derived from a 5-m Digital Terrain Model (DTM). The map indicates the surface traces of the BM and Mixcoac faults, seismic events, station locations, and main streets. The beach balls show the focal mechanisms determined for both faults from the simulated annealing inversions, and the dashed gray lines indicate the geomorphic extension of the faults to the west. The blue triangles show the seismic stations used to detect template matching (TM) earthquakes and the gray triangles show other stations used to locate the December 14 earthquake. The dashed rectangle delineates the area analyzed for slope orientation shown in the inset. Inset figure: Detailed analysis of the aspect and slope (in degrees) of landscape slopes within the dashed rectangle. (a) shows the aspect and slope of all pixels, while (b) highlights pixels with slopes greater than 20 degrees. Green arrows indicate the preferential orientation of fault planes for the Barranca del Muerto and Mixcoac faults as determined in this study. (For interpretation of the references to colour in this figure legend, the reader is referred to the web version of this article.)

wells (Cappa et al., 2019; Ge and Saar, 2022; Guglielmi et al., 2015; Larochelle et al., 2021), and where advanced InSAR imaging has been critical to characterize the associated surface deformation (Eyre et al., 2022; Pepin et al., 2022; Srijayanthi et al., 2022). In those cases where seismic swarms are accompanied by slow slip, the seismic moment accumulated by the seismicity is only a small fraction (<10 %) of the geodetically determined seismic moment released in the fault system (Jiang et al., 2015; Jiang et al., 2022; Pepin et al., 2022; Wicks et al., 2011).

The Valley of Mexico basin is subject to massive groundwater extraction to meet ~50 % of the needs of more than 9 million people. This translates into one of the highest ground subsidence rates in the world (i.e., up to 500 mm/year) (Cabral-Cano et al., 2008; Chaussard et al., 2021; López-Quiroz et al., 2009; Ortega-Guerrero et al., 1999). Such subtraction of groundwater produces pore pressure gradients and, therefore, a sustained underground fluid diffusion structurally conditioned by local fracture systems that may preferentially induce normal faulting (Foulger et al., 2018; Moein et al., 2023; Segall, 1989).

On May 11, 2023, an Mw3.2 local earthquake (700 m depth) occurred in the west part of the city (Fig. 1), producing strong intensities in the epicentral zone (Quintanar et al., 2024). This earthquake was the largest of a seismic swarm that began in February about 5 km south of the 2019 crisis, and less than 2 km from the 1981 swarm (Fig. 1). Seven months later, on December 14, a similar Mw3.2 event (500 m depth) occurred 1 km north accompanied by preceding and subsequent earthquakes until at least May 2024. Ground shaking again caused great concern among the population and some damage to buildings near the epicenter. In the following days, the national media even reported fracture alignments in nearby streets.

Based on unprecedented satellite interferograms and detailed analysis of both microseismicity and local terrain geomorphology, in this work we explore the origin of local seismicity and show that two north-facing normal faults below the western part of Mexico City experiencing slow aseismic slip played an important role throughout the months-long seismic crisis of 2023 and 2024.

2. Results

2.1. Geomorphology of the West Bank of Mexico City

Outcrops displaying current or historical geological structures evidencing normal faulting atop the 2023–2024 seismic sequence, which occurred in a relatively flat area, are virtually nonexistent. Hypocentral locations reported by Quintanar et al. (2024) indicate that seismicity occurs at shallow depths (<1.5 km). However, the active faults are buried beneath Quaternary sediments corresponding to the transition from rocky hills to clay-rich lake-bed deposits. Consequently, there is little to no evidence of event-related scarps formed along these faults visible on the surface (i.e., they are blind faults), also because they are beneath a heavily urbanized area where any unaltered paleo-scarps were likely leveled for construction erasing any direct evidence of displacements along these faults.

Less-urbanized hilly areas in the western bank of the city, just a few hundred meters west of the 2023–2024 seismic sequences, have been the focus of various regional studies, as they provide a more suitable setting for finding evidence of historical faulting (e.g., Vásquez et al., 2021). These hilly areas show evidence of soil erosion due to the action of running water. Although detailed geological mapping is limited, SW-NE normal faulting has been reported, supported by the interpretation of stereographic pairs of aerial photographs (Arce et al., 2015). Focal mechanism interpretations of comprehensive seismological records roughly align with the orientation of photo-interpreted fault scarps (Havskov, 1982; Lermo et al., 2016; Quintanar et al., 2024; Singh et al., 2020). However, orientations provided by these interpretations are somewhat imprecise, and orientation solutions provided by focal mechanisms prior to the gradual installation of the broadband seismic

network “Red Sísmica del Valle de México” of the Mexican Seismological Service (SSN) (Quintanar et al., 2018) are limited as well.

“Slope” is a term used in two contexts. The first refers to the steepness of any surface, while the second refers to a specific landform element. Slopes are fundamental landforms characterized by inclined surfaces that connect higher and lower elevations. We utilize abundant data from a high-resolution digital elevation model (DEM) (Instituto Nacional de Estadística y Geografía, INEGI, 2024) to conduct a robust and straight-forward analysis of slope orientation and steepness in the hilly sector west of the earthquake sequence. Given that erosion rates are lower than the tectonic processes associated with normal faulting in the area, the wealth of data available from the DEM can capture any statistical tendencies of the preferential directions of slopes that, as we shall demonstrate later, are produced by normal faulting. Our analysis relies on a lidar-derived high-resolution (5 m pixel-size) digital terrain model (DTM) (Instituto Nacional de Estadística y Geografía, 2024). We conduct our analysis in three main steps as described below.

In the first step, we calculate the orientation and steepness of the landscape slopes in the area using the Aspect and Slope workflows available in QGIS 3.12.1 (QGIS Project, 2024). Aspect calculates the relief’s azimuth measured clockwise from true north, indicating the direction towards which the topography faces, whereas Slope calculates the steepness of the topography measured from a horizontal plane. With these two calculations, we obtain the orientations and steepness of all pixels in the area, which range from 0° to 360° and 0° to 90°, respectively. However, to proceed with our analysis, we need to distinguish landscape slopes from other landforms (e.g., valleys, ridges, spurs, etc.) and anthropogenic structures captured by the DTM.

In the second step, we apply a classification algorithm to identify landforms in our study area, allowing us to discriminate landscape slopes. We use a texture-based pattern recognition approach, which exploits the concept of geomorphologic phenotypes, or geomorphons, to classify landforms (Stepinski and Jasiewicz, 2011). Geomorphons allow a systematic treatment of pixel neighborhoods to identify terrain features using DEMs, leading to precise and adaptable mapping of landforms (Jasiewicz and Stepinski, 2013). We use the geomorphons workflow developed by Stepinski and Jasiewicz (2011) and implemented in GRASS (GRASS Development Team, 2022). To retain the fine details available from the high-resolution DTM, we use a search distance of 3 pixels and an angle tolerance of 4 degrees. Finally, we produce a mask to identify pixels classified as landscape slopes. The orientation (aspect) of these pixels (i.e., the orientation of slopes) is shown in Fig. 1 with background colors.

In the third step of our analysis, we use the mask of landscape slopes on the orientation and steepness layers to perform a pixel-wise statistical analysis of the orientation and steepness of the landforms classified as slopes (inset histograms in Fig. 1).

From the map of terrain orientation (Fig. 1), we observe that landscape slopes predominantly face towards the NW and SE quadrants. This observation aligns with previously reported NE-SW alignments of photo-interpreted fault traces and focal mechanism analyses (Arce et al., 2019). The frequency analysis of slope orientation (inset panel a in Fig. 1) indicates that slopes are primarily oriented towards the SE in a subregion west of the 2023 earthquakes and the two normal faults identified later in this study (dashed rectangle box). The distribution of steepness per class, shown in colour within the petals, reveals that most slopes have an inclination of less than 20° (inset panel a). However, a focused analysis of slopes with a steepness greater than 20° (inset panel b) shows a dominant, well-defined modal class oriented towards the N-NW, which is consistent with the dip directions of the two normal faults (green arrows, inset panel b). As we will justify later when modeling unprecedented satellite images of the ground deformation, we interpret these landscape slopes as a surficial manifestation of faults tectonic activity. We infer that the prevalence of slopes with steepness lower than 20° is due to erosion, while slopes greater than 20° represent more recent, less-eroded parallel and subparallel fault scarps.

2.2. Tectonic-related InSAR deformations

The systematic search for ground displacements in Mexico City has long been the aim of different groups, mainly to assess the well-known land subsidence at scales both regional (Cabral-Cano et al., 2008; Chaussard et al., 2021; López-Quiroz et al., 2009; Osmanoğlu et al., 2011) and local (Solano-Rojas et al., 2020). Our current understanding of this phenomenon on a local scale comes mainly from the analysis of satellite radar interferometry, which can identify the large ground displacements (up to 500 mm/yr) resulting from subsidence due to aggressive groundwater extraction (Khorrami et al., 2023). However, as mentioned earlier, the Valley of Mexico lies in the TMVB (Fig. 1), a tectonically active region where shallow, potentially harmful earthquakes occur (Suárez et al., 2019, 2020). Local seismicity in Mexico City has been studied since 1909 (Figuerao, 1971) with magnitudes of less than 4. As the earthquakes are relatively small, the associated surface deformations have been likely neglectable or even masked by subsidence, until now. As a result of a systematic search in Mexico for earthquake-related signals using Sentinel-1 satellite SAR images, in the following we present the first evidence of two tectonic-related signals found in the very heart of the city, which occurred in May and December 2023 during a long-lasting seismic crisis. The subsidence signals in the area do not overlap with those from microearthquakes, as shown in Supplementary Fig. S2f, g.

Satellite Interferometric SAR (InSAR) has enabled the observation of ground displacements across a variety of spatial and temporal scales (Elliott et al., 2016). For example, InSAR has been successfully used to observe signals from small interplate earthquakes, such as the 1992–2022 Zagros (southern Iran) earthquakes with $M_w > 4.5$ and depths as shallow as 0.7 km, showing amplitudes of ~ 2 cm using ERS-1 and 2C-band satellites (Lohman and Simons, 2005), or even large earthquakes in Mexico (Villafuerte et al., 2025; Wen et al., 2021). Reportedly, the long temporal baselines available at that time impeded precise dating of earthquakes and induced decorrelation, hindering the observation of signals from shallow, lower-magnitude earthquakes in the region (Lohman and Simons, 2005). No-tectonic events have shown the potential of short temporal baselines (12 days) available from Sentinel-1 to observe cumulative displacement signals like such in Jamnagar, India, where a rainfall-related swarm of 76 microearthquakes, over 70 % of which were magnitude < 3 with depths < 5 km, produced signals with amplitudes of ~ 2 cm (Srijayanthi et al., 2022). We therefore profit from the short revisit time available from the Sentinel-1 mission to conduct an analysis to constrain in time and space any earthquake-related signals in Mexico City.

We first focus on the May 11 and December 14, 2023, earthquakes, selecting pairs of Sentinel-1 SAR scenes to produce interferograms with the shortest possible temporal baselines (Supplementary Fig. S1). To produce the interferograms, we use the InSAR Scientific Computing Environment (ISCE) (Rosen et al., 2012), applying multilooking to achieve a pixel size of ~ 30 m and performing a topographic phase correction using a 30 m SRTM DEM (Farr et al., 2007). For the May 11 event, we use scenes acquired on May 9 and May 21 in ascending orbit, and on May 6 and 18 in descending orbit. For the December 14 event, we use scenes acquired on December 8 and 20 in ascending orbit, and on December 11 and 23 in descending orbit (middle column of Supplementary Fig. S1).

Although atmospheric noise is present in the May ascending orbit interferogram, we indeed observe signals typically related to normal faulting in all the interferograms (Fig. 2, left column). To ensure the coseismic interferograms accurately depict signals constrained in time and are not a result of regional subsidence, or merely topography-related atmospheric noise, we calculate two pre-seismic and two post-seismic 12-day interferograms for each event and orbit (first two and last two columns in Fig. S1). We confirm that the signals observed in the coseismic interferograms are absent in the pre- and post-seismic interferograms, although atmospheric noise persists in the May ascending

orbit post-seismic interferograms. We additionally observe that the general trend of the signals we found align quite well with the morphology orientations we determined in the previous section (compare Fig. 1 with Fig. 2). We, thus, obtain one interferogram with a clear co-seismic signal for May, and two for December.

We perform an additional examination of the ascending orbit December interferograms to further constrain the timing of the coseismic signal (Fig. S2). We produce a 24-day interferogram using scenes acquired from November 12 to December 23. Fig. S2 (panels a,c versus b,d) presents the wrapped and unwrapped phases of this 24-day interferogram alongside the corresponding phases from the previously obtained 12-day ascending orbit interferogram using scenes from December 11 and 23. We then obtain the difference between the two unwrapped interferograms to produce Fig. S2e. Since both interferograms share the December 23 scene, any residuals would represent a signal originating between November 12 and December 11. We find, however, a negligible residual between the two interferograms, indicating no evidence of deformation before December 11, i.e., three days prior to the mainshock of December 14.

At this point, we have established that co-seismic signals can be observed in the 12-day interferograms generated for the Mw3.2 May and December 2023 shallow earthquakes. To ensure comprehensive coverage of relevant signals for our study, we used the SSN event catalog (“SSN Catálogo de Sismos UNAM”, 2023) to search for displacements related to similar shallow, small magnitude ($M_w < 3.5$) intraplate earthquakes occurring in the last six years within the city, including an Mw3.2 earthquake of July 2019 (Fig. 1) (Singh et al., 2020). We present the resulting 6-day and 12-day co-seismic interferograms corresponding to the reported event in Fig. S3. No additional signals indicating earthquake-related co-seismic deformation were observed. Several factors may contribute to this observation: atmospheric noise present in several interferograms, uncertain earthquake magnitudes, underestimated depths, and potentially thicker clay-rich deposits where the inspected earthquakes occurred compared to the May and December 2023 earthquakes, which were in transition areas with thinner overlying sedimentary deposits.

We thus proceed with the three coseismic interferograms we obtained, where signals are observed. Due to the abundance of data available from the interferograms, and as an additional measure to reduce high-frequency noise in the recovered signal, some downsampling is in order. For downsampling the data, we used the saliency-based quadtree algorithm (SQS) (Gao et al., 2021), a convenient technique allowing to reduce the data volume while preserving significant information. Saliency is a property of any image that reflects the relevance of the information to the human eye, which makes it a powerful mean to identify surface deformations with respect to its surroundings (Gao et al., 2021). This parameter helps to differentiate between the near-field (i.e., the deformation zone) and far-field (i.e., the areas unaffected by faulting). While regions with higher saliency values (indicating more significant deformation) are selected for denser sampling, the regions with lower saliency values are sampled sparsely or even excluded. We present the corresponding Saliency values obtained for the three coseismic interferograms in question (Fig. S4), which are used to determine the density of the quadtree data sampling. The right column of Fig. 2 presents the resampled interferograms for the May and December 2024 events, which will then be used to determine the faults that gave rise to surface displacement signals.

2.3. Faults mechanism and location

The study region lies in the foothills of the “Sierra de las Cruces” mountain range. According to Arce et al. (2019), the fault system that dominates this region has a NE-SW strike direction. The detailed geomorphological analysis of Section 2.1 indicates that topographic slopes facing north have dominant trend around $252 \pm 15^\circ$ (derived from the inset of Fig. 1) west of the 2023 earthquakes, which is close to the

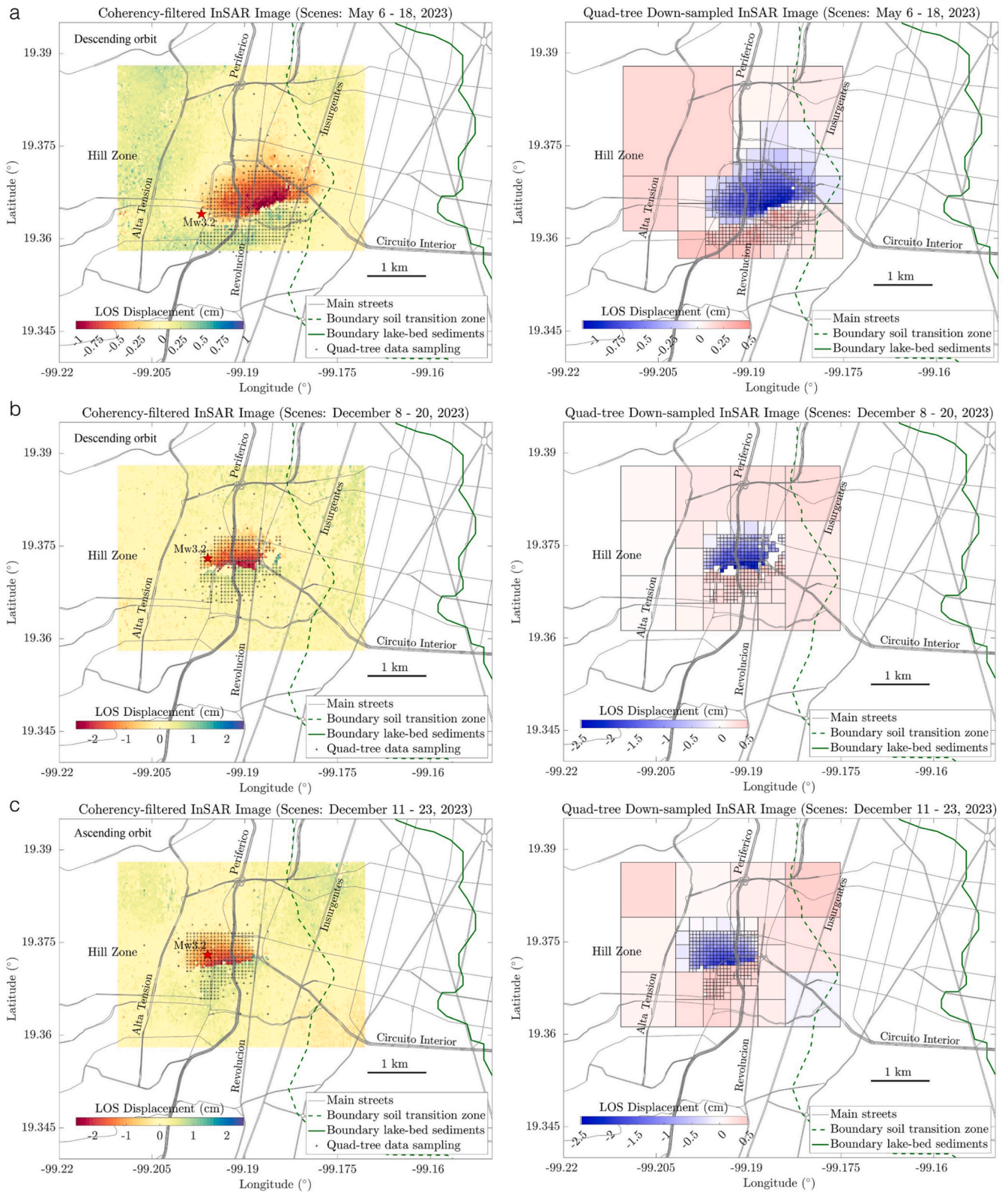


Fig. 2. 12-day Sentinel-1 coseismic interferograms and Saliency-Based Quadtree Sampling (SQS). Dates used for generating each interferogram are specified in the upper part of each pane. (a) Coseismic interferogram and SQS for the May 11, 2023 event. (b) and (c) Coseismic interferograms and corresponding SQS obtained from ascending and descending orbits, respectively, for the December 14, 2023 event.

normal fault mechanism determined by Quintanar et al. (2024) for the Mw3.2 earthquake of May 11, with strike of 270° . However, a visual inspection of the May interferogram (Fig. 2a) suggests that the polarity

reversal contour is closer to the topographic trend found statistically, as it is also visible in the December interferograms (Fig. 2b-c).

Determining the location and mechanism of the faults responsible for

the observed ground deformation is essential to retrieve the associated slip distributions reliably. For this reason, we performed a robust and comprehensive analysis of the InSAR data based on a fault model with the minimum number of parameters possible. The aim is to explain the data from a simple circular dislocation as well as possible. The problem reduces then to determining the direction of the slip in space (i.e., strike, dip, and rake angles), the fault center position (i.e., latitude, longitude, and depth), the circle parameters (the radius and its along-dip fault position), and a factor that scales the slip. This means a source model with nine parameters. Since the fault cannot extend to the surface due to limitations of our model, given 100 m long square sub-elements, the fault dimension is automatically adjusted during the inversion procedure explained below, so that it is truncated as close to the surface as possible. Fig. S5 illustrates the model geometry. The slip distribution on the circular patch is dictated by a centered ellipsoidal function whose semiaxis is adapted automatically so that the slip is negligible at the perimeter of the source. To estimate the LOS displacements at the surface from a given slip model, we used the Okada (1985) formulation for a homogeneous half-space.

The crustal structure below the Valle of Mexico is characterized by a ~ 2 km thick uppermost layer with shear wave speed around 1.5 km/s

that correspond to the southernmost part of the Mexican Volcanic Belt (Cruz-Atienza et al., 2010). This heterogeneous geologic unit consists of a series of andesites and volcanic tuffs intermixed with sands, shales, sandstones, lacustrine limestones, breccias, and conglomerates. Our study area extends over a soil transition composed of alluvial and clay deposits, so the elastic properties we adopted for the whole study are $V_P = 2785$ m/s, $V_S = 1608$ m/s, and $\rho = 2200$ kg/m³, which were taken from a local tomography derived from the joint inversion of receiver functions and surface waves dispersion curves (Aguilar-Velázquez et al., 2023, 2024).

To find the fault model optimal parameters, we applied a Simulated Annealing (SA) method (Corana et al., 1987) that minimizes the mean absolute percentage difference between the observed and synthetic LOS displacements following the quad-tree data sampling introduced in Section 2.2. Unlike the May event where only one interferogram is available (Fig. 2a), the December event was modeled from the joint inversion of two LOS components (Fig. 2b and c).

We conducted 54 independent optimizations per event, each with 125 iterations. The algorithm by Corana et al. (1987) involves multiple explorations per parameter and per iteration, so we set the algorithm to do 10 explorations. This resulted in a total of 607,500 explored models

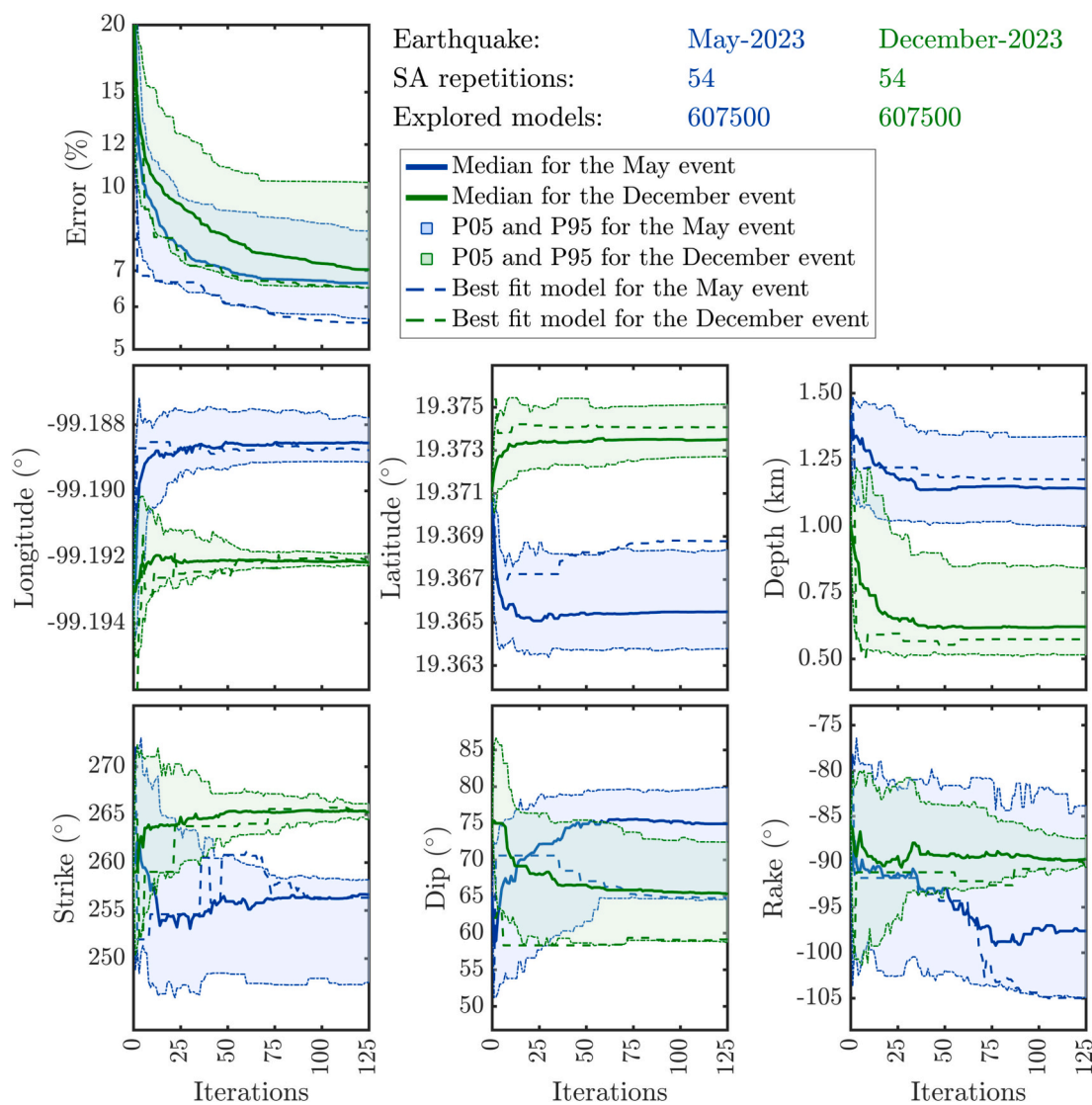


Fig. 3. Misfit error evolution and fault parameters convergence during the Simulated Annealing inversions of InSAR data for the May (blue) and December (green) events on the Barranca del Muerto and Mixcoac faults, respectively. See Section 2.3 and Fig. S5 for the problem geometry. (For interpretation of the references to colour in this figure legend, the reader is referred to the web version of this article.)

per event that were combined for the analysis. Fig. 3 illustrates the convergence of the most relevant model parameters for the May (blue curves) and December (green curves) events, where the solid lines depict the median values, the colored regions indicate the range from the first to the third quartile, and the dashed lines correspond to the optimal models.

Overall, the inversions of both events converged on two steeply dipping east-west trending normal faults that are consistent with each other (see Table 1) and with the moment tensor inversions of local earthquakes (L Quintanar et al., 2024; Singh et al., 2020). After careful consideration including the geological literature, we will refer to these faults hereafter as the Barranca del Muerto (BM) fault to the south and the Mixcoac fault to the north (Fig. 1). The optimal strikes found of 256° and 265° for the BM and Mixcoac faults (Table 1), respectively, are also consistent with the $252 \pm 15^\circ$ trend determined statistically from our independent geomorphological analysis in Section 2.1 (Fig. 1). As expected, the joint inversion of two LOS components for the December event converged better than for the May event, where the interquartile ranges for some parameters remained relatively wide (e.g., the rake angle). Since the May event is less constrained, the misfit function was minimized much faster and the optimal model parameters are in some cases outside the interquartile ranges. Fault locations on the other hand converged rapidly in both cases (i.e., after ~ 15 iterations). Figs. S6, S7 and S8 show the optimal fault solutions, reported in Table 1, together with the data misfits for the three interferograms concerned that we adopted to perform the detailed slip inversions in the next section.

2.4. Slip inversion from InSAR data

From the exercise above, we constrained the most relevant fault parameters: the fault mechanism and location. For that purpose, we used an inversion strategy that explains the broad features of the InSAR data based on simple slip models. In this section, we adopt those optimal fault attributes (Table 1) to perform a detailed slip inversion of both events using the ELastostatic ADjoint INversion (ELADIN) method (Tago et al., 2021), a recently developed strategy that honors physically consistent restrictions (i.e., rake angle and von Karman slip distributions) via a gradient projection method.

The faults were discretized with 100 m length square subfaults and the inversions performed assuming a von Karman correlation length of 200 m. In both faults, the rake angle could vary about 20 % from the optimal value. Since the Okada (1985) model used to generate the Somigliana Green's functions does not allow the fault to reach the free surface, the tops of the shallowest subfaults lie around 30 m below the surface. To assess the inverse problem resolution, Figs. S9 and S10 show the mobile checkerboard (MOC) tests (Tago et al., 2021) for the BM and Mixcoac faults, respectively. The tests reported correspond approximately to the minimum-resolvable asperity size in each case, which is 900 m for the May event, where only one interferogram is available (Fig. 2a), and 600 m for the December event, where two LOS displacement components were inverted simultaneously (Fig. 2b-c). The number of combined synthetic inversions per MOC test is 14 and 16, respectively. Average restitution indexes (ARI), which are a slip resolution metric independent of the checkerboard position, correspond to 0.86 ± 0.1 in average above 1.5 km depth for the May event (Fig. S9a), and 0.83 ± 0.11 above 1 km depth for the December event (Fig. S10a). This

means that nominal errors in those fault segments are below $\sim 16\%$ and $\sim 17\%$ as compared to the actual fault slip. However, although fit errors are minimal (panels d), an inspection of individual checkerboard inversions reveals that slip solutions below ~ 800 m in both cases are affected by smearing effects due to the inverse problem sensitivity, which makes slip patches to appear slightly deeper than they are (panels b and c). Thus, subsequent data interpretation at depth should consider this modeling limitation.

Fig. 4 shows the slip inversions for both events assuming the same model parameterization as for the MOC tests. While no slip penalization was used in the Mixcoac fault, solutions were penalized below 1.5 km to mitigate deep unresolved slip in the BM fault. The data fit is very satisfactory, as shown along two profiles on the major asperities together with the standard deviations within a 400 m profiles vicinity (panels b and e). The standard deviation of the overall error are 0.171 cm and 0.183 cm for the May and December events, respectively, while the mean values are close to zero in both cases (panels c and f). Such small data misfits were expected given the results achieved in the previous section, where the problem geometry was optimized while fitting the same data (Figs. S6-S8).

The slip distribution for the May event on the BM fault features a prominent asperity between 0.5 and 1.5 km depth with a maximum slip of 7 cm that extends to the west while getting thinner and shallower (Fig. 4a). Surprisingly, slip to the west surrounds the hypocentral region of the Mw3.2 earthquake of May 11, which can also be appreciated in the three-dimensional representations of Fig. 5b-c. This means that the surface deformation pattern observed between May 6 and May 18 (Fig. 2a) is explained by an extended deep asperity about 1 km east of the earthquake (i.e., just below Revolucion Street, which runs above Line 7 of the Mexico City underground metro) and a much smaller slip strip reaching the earthquake hypocenter west of the Periferico Main Street, which may correspond to the coseismic and postseismic slip signature of the event. The moment magnitude of the slip distribution is $M_w = 4.1$, which means that the associated scalar moment is 22 times larger than the mainshock corresponding value. Relocated seismicity between March and July 2023 reported by Quintanar et al. (2024) (dark blue dots, Fig. 4a) and template matching (TM) detections in May (light blue dots), which will be properly introduced in the next section, are distributed over and around the fault.

Regarding the inversion for the December event on the Mixcoac fault, Fig. 4d shows that the slip concentrated in a much shallower fault region (i.e., above 0.9 km depth) and likely reached the earth's surface. Indeed, days after the Mw3.2 earthquake of December 14, several public media reported aligned fractures in the streets around the surface projection of the fault (green line). The slip pattern is composed by two interconnected asperities with higher overall slip than found for the May event, with a maximum of 8 cm about 400 m depth in the eastern asperity (i.e., east of the Periferico Main Street) and total moment magnitude $M_w = 3.9$, i.e. a scalar moment 11 times larger than the mainshock corresponding value. Precise enough location of the mainshock to determine whether it occurred on the fault is a difficult task that we shall discuss in detail on section 2.6. On the other hand, double-difference relocated earthquakes from December 2023 to May 2024 (blue dots), first reported here, show that most of the events fall west of the fault (i.e., west of the Periferico Main Street) with some exceptions near its eastern end. Based on this seismic evidence, the peculiar two-

Table 1

Locations and focal mechanisms of the two 2023 mainshocks and the Barranca del Muerto and Mixcoac faults. The latitude, longitude and depth of the faults correspond to the center of the faults. *Location and fault mechanism by Quintanar et al., 2024.

	Latitude (°)	Longitude (°)	Depth (km)	Wide (km)	Length (km)	Strike (°)	Dip (°)	Rake (°)
May 11 earthquake*	19.364	-99.197	0.70	-	-	270	76	-75
December 14 earthquake	19.373	-99.197	0.50	-	-	259	89	-86
Barranca del Muerto fault	19.369	-99.189	1.18	2.6	2.6	256.3	64.8	-105
Mixcoac fault	19.374	-99.192	0.57	1.6	1.6	265.1	59.2	-90.3

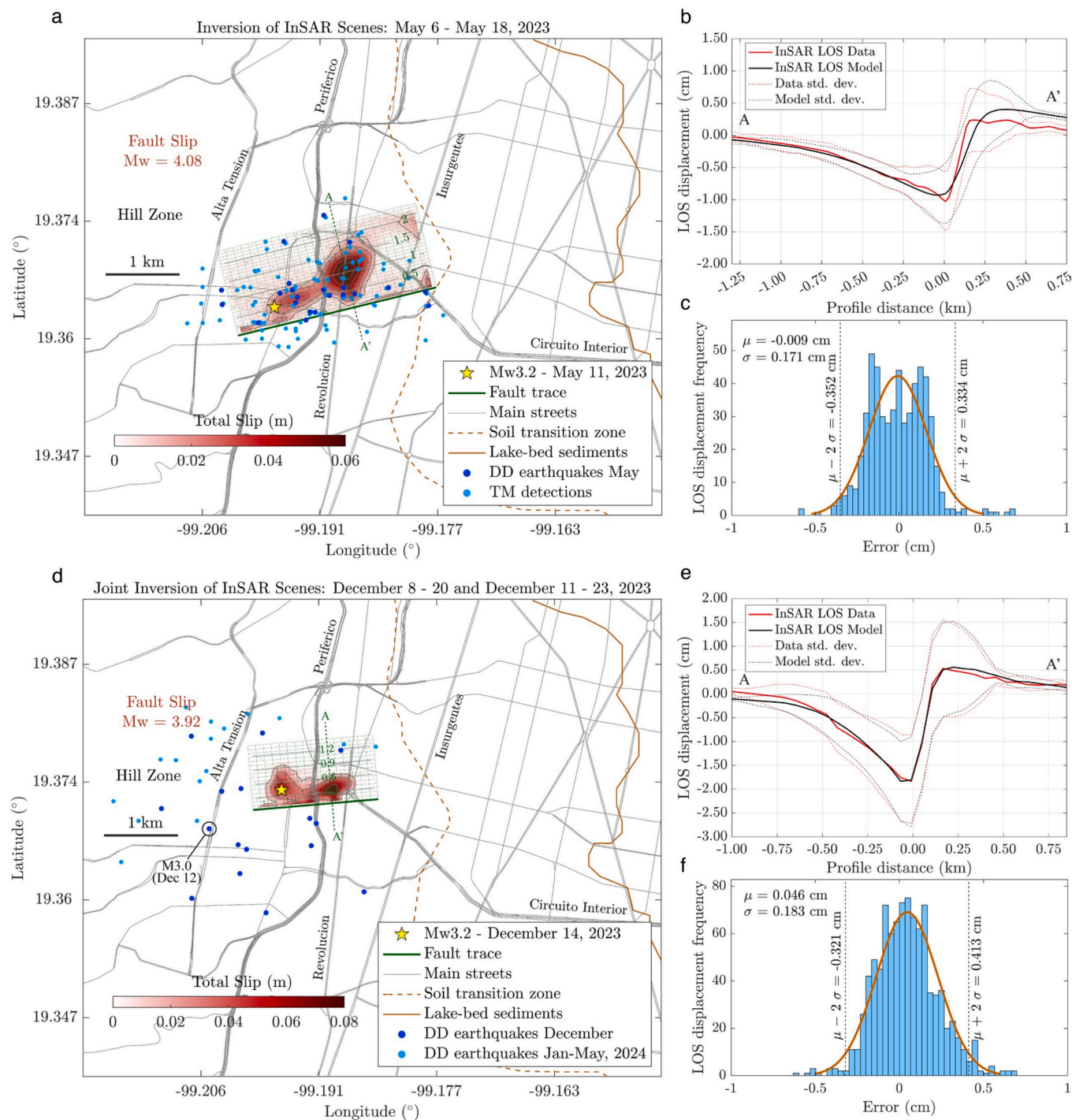


Fig. 4. Slip inversions from InSAR data of the May and December events on the Barranca del Muerto (a) and Mixcoac (d) faults by means of the ELADIN method. Comparison of the data and the model predictions within 400 m from the two A-A' profiles are shown in (b) and (e), and the inversions error distributions in (c) and (f).

lobe slip distribution and two stronger arguments given in Section 2.6, we believe that the western fault asperity may correspond to the coseismic and postseismic signatures of the December 14 mainshock.

A three-dimensional rendering of the slip solutions on both faults is shown in Fig. 5 (and Supplementary Movie S1), where we also included our high-resolution DEM scaled by a factor of four to appreciate better the geomorphological features, which were statistically characterized in Section 2.1 and have a local direction of $342 \pm 15^\circ$ for the steepest slopes (see inset of Fig. 1). A clear structural connection comes out between both normal faults and two north-facing cliffs emerging to the west from

the Periferico Main Street, suggesting that these cliffs, delineated with dashed gray lines in Fig. 1, are the geomorphic westward expression of the buried faults to the east. This structural connection is particularly important because it rules out other mechanisms that could produce similar InSAR deformation patterns, such as anthropogenic activity (e.g., water extraction) and city infrastructure.

2.5. Seismicity and Slow Slip in the Barranca del Muerto Fault

The slip inversions introduced above represent the time integration

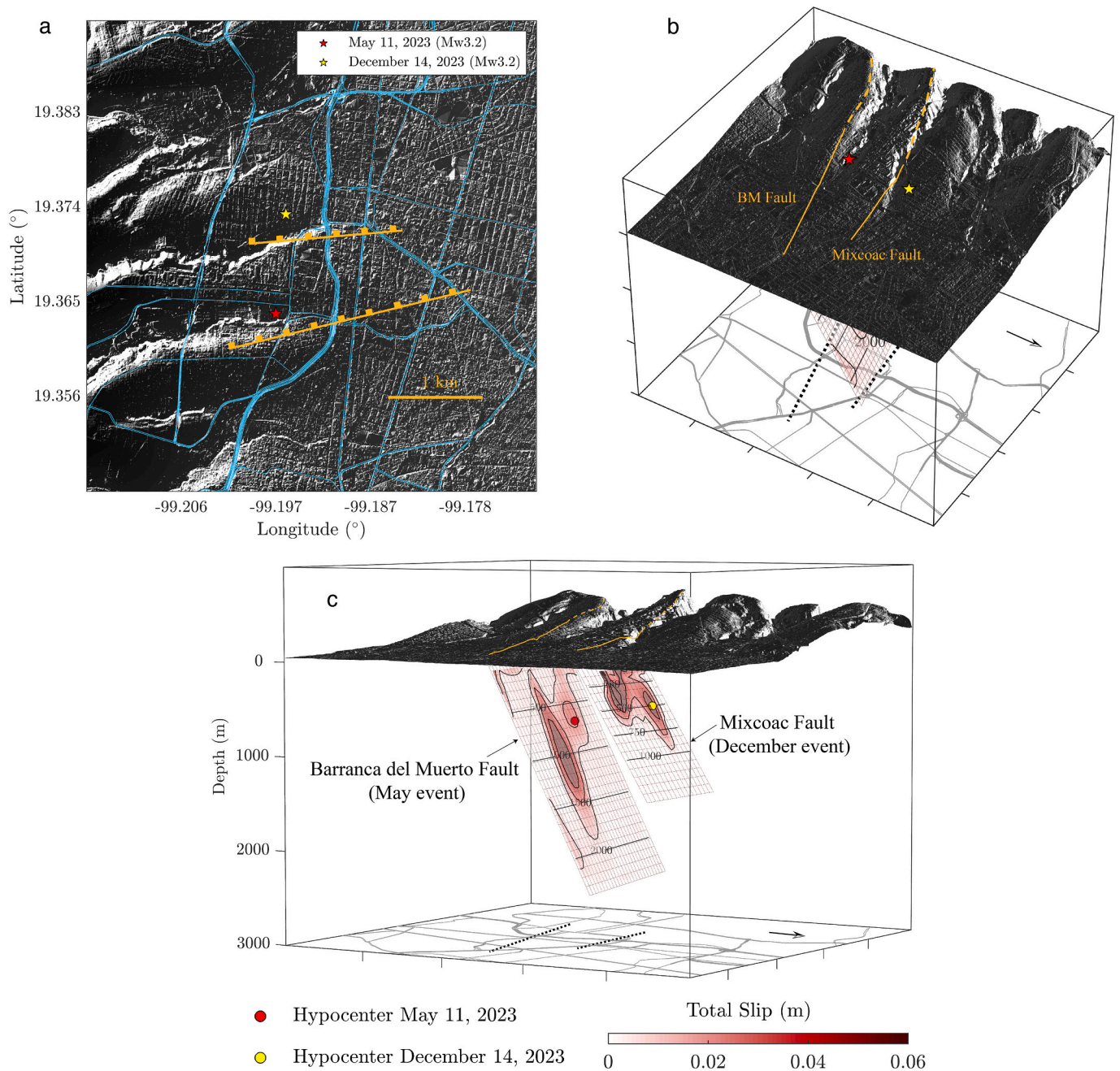


Fig. 5. Three-dimensional rendering of the InSAR inverted slip on the Barranca del Muerto and Mixcoac faults. Notice the structural connection between both blind faults and two north-facing cliffs west from them. The blue curves in (a) show the Mexico City main streets. The topographic relief is exaggerated four times. (For interpretation of the references to colour in this figure legend, the reader is referred to the web version of this article.)

of the fault slip history between the two dates where the InSAR scenes were taken. So, nothing can be said about the timeline involving the mainshocks and the faults slip evolution. For instance, the interferogram used to model the May event (Fig. 2a) and the associated slip (Fig. 4a) include everything that happened on the fault during 12 days between May 6 and May 18. Since the Mw3.2 earthquake occurred on May 11, slip could initiate during the 6 days preceding the earthquake. In the past, local earthquakes in the western part of the city were reported as seismic swarms that may last for months before a mainshock. This was the case of the 1981 and 2019 earthquakes (Havskov, 1982; Singh et al., 2020). For the 2023 crisis, Quintanar et al. (2024) reported that seismic activity was initiated in February and continued until the mainshock occurred on May 11, indicating that fractures' instability and interaction across a fault system occurred during weeks to month-long periods,

certainly driven by some underlying local process.

To assess whether aseismic slip was initiated in the BM fault before the mainshock, we used a template matching (TM) technique (Liu et al., 2020) to detect small local earthquakes with low signal-to-noise ratio, which is particularly convenient within urban areas. As templates, we used the waveforms from a double-difference (DD) relocated catalog reported by Quintanar et al. (2024) shown in Fig. 4a (dark blue dots), which contains 22 well-located earthquakes. We applied the TM technique to estimate the stacked correlation coefficient for each of the templates and the continuous recording for three local stations (PZIG, ENP8 and BJVM; Fig. 1) from May 1 through May 31. The TM performs a continuous search by computing the correlation coefficient between the templates and the continuous data at each sample step. A detection is declared when the correlation coefficient exceeds n times the mean

average deviation (MAD) of the correlation coefficient for each day. By visually inspecting the detections obtained for different MAD threshold values, we empirically determined that $MAD \geq 9.2$ provides a robust and reliable catalog with 89 detections in May above the threshold. Fig. 6a-b shows a comparison between two templates and the continuous data for two previously unreported earthquakes with $MAD = 17.15$ and $MAD = 9.26$, respectively. Examples for higher MAD values are shown in Fig. S11. The magnitude of the detections was estimated by comparing the median of the relative amplitude between the peak values of the template and the detection (Liu et al., 2020). To precisely locate the events, templates are allowed to move from their position in a cubical regular grid (Supplement Fig. S12). By estimating the delayed times for each grid point based on the local velocity model used for this study (Section 2.3), correlation coefficients are computed for the whole lattice and the final location corresponds to the largest correlation coefficient. In this case, we used a grid around the template location with $\pm 0.004^\circ$ length in latitude and longitude, and ± 100 m vertically, with grid increments of $\pm 0.002^\circ$ and ± 50 m, respectively. In summary, we

tested 27 possible foci around each template in addition to the template location. Fig. 6c shows the temporary evolution of the seismic catalog, where orange stems indicate the time and magnitude of the templates, while blue stems correspond to the TM detections. A similar timeline representation is shown in Fig. 6d and e in terms of the events depth and MAD values. The magnitude frequency distribution is shown in Fig. S13 including the DD and TM catalogs, which resulted in the 89-event catalog with a magnitude range between 0.2 and 3.2, a magnitude of completeness $M_c = 1.2$, and a standard b-value of 1.01 ± 0.33 (Fig. S13). Fig. 6d-e shows the events depth distribution versus time colour coded by magnitude and MAD value, respectively. High MAD values above 25 correspond to the templates (i.e., $CC = 1$).

Fig. 7a-b shows two perspectives of the fault slip together with our TM catalog for May (see Supplementary Movie S2). Despite the uncertainties in the foci, which we estimate of the order of ± 100 m given the TM grid size, the spatial correlation between the seismicity and the slip distribution is remarkable. While earthquakes around the main-shock hypocenter (yellow dot) to the west are above ~ 800 m, events to

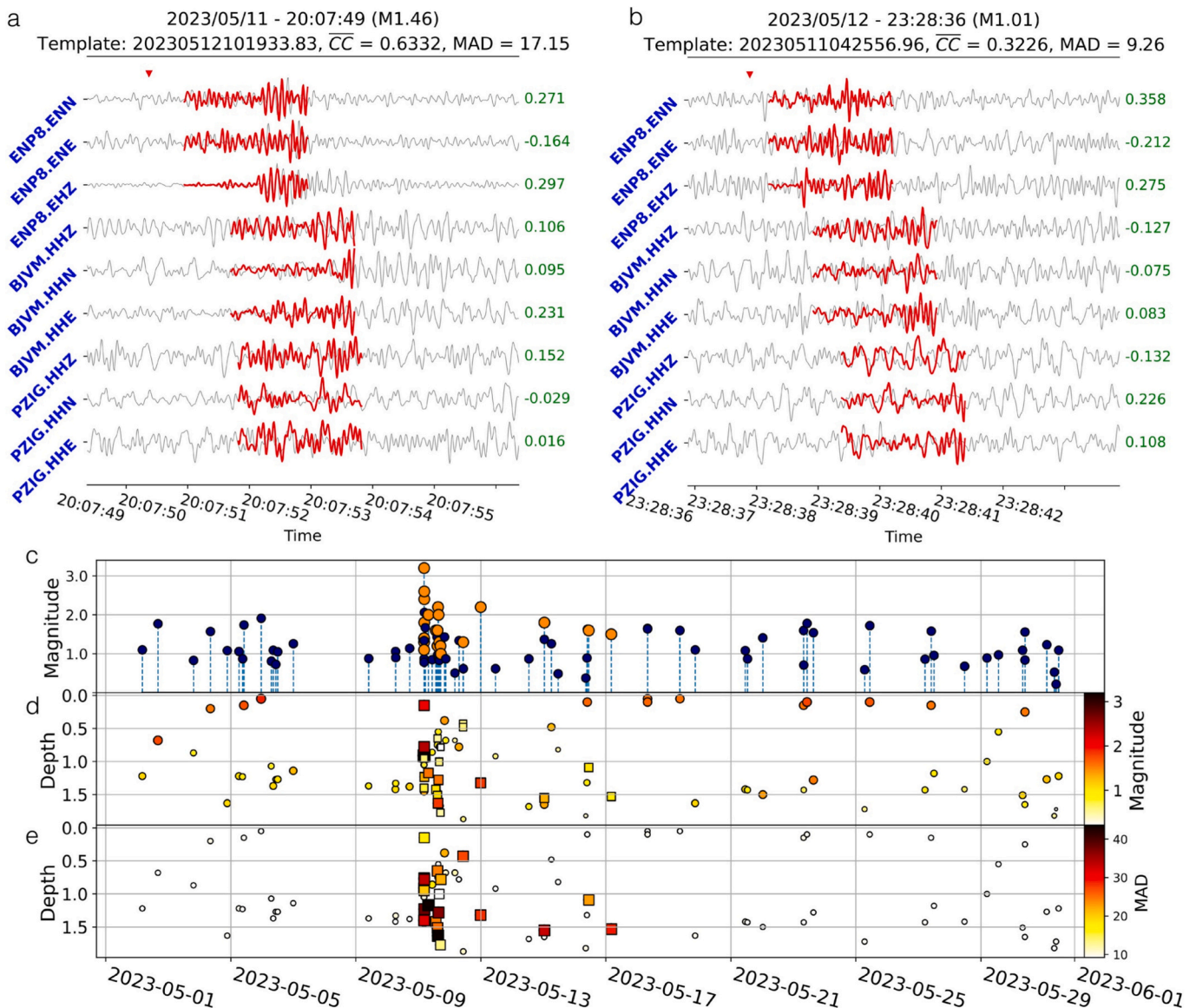


Fig. 6. Template matching detections. (a) and (b) shows the comparison between the template (red lines) and the continuous recording (gray lines) for two events detected using the TM with MAD of 17.15 and 9.26, respectively. (c) shows the temporary evolution of the catalog from May 1st through 31st, templates are shown in orange and TM detections in blue. (d) and (e) indicates the depth distribution of the detections. (For interpretation of the references to colour in this figure legend, the reader is referred to the web version of this article.)

the east concentrate in a deeper region, between 600 and 1400 m depth, as does the slip pattern. Based on this spatial correlation while considering the foci and slip uncertainties, we will focus only on seismicity rate variations along the fault strike and above the completeness magnitude $M_c = 1.2$ (Fig. S13) in the following. To this purpose, regardless of the events depth, we projected horizontally the hypocenters into the fault plane following a strike-perpendicular direction. Fig. 7c shows the timing of all detections above M_c as a function of the along-strike distance from the mainshock hypocenter. Blue dots indicate foreshocks and red dots indicate aftershocks. The gray band depicts the time between both InSAR scenes used to invert the fault slip. To have a rough estimate of the earthquakes' size and their average slip, \bar{d} , for a circular crack with stress drop $\Delta\tau$ and radius r we have $\bar{d} = \frac{M_0}{\mu\pi r^2}$ and, given Eshelby's (1957) solution for this problem, $r = \sqrt[3]{\frac{7}{16} \cdot \frac{M_0}{\Delta\tau}}$, where M_0 is the scalar moment and μ is the shear modulus of our velocity model (Section 2.3). Given the magnitude of each detection and assuming a stress drop $\Delta\tau =$

0.5 MPa, as determined for the mainshock by Quintanar et al. (2024), then we have d and r for each event, as shown in Fig. 7c with horizontal bracket bars for the source lengths. To estimate the scalar moments, we assumed that the magnitudes, derived by comparing the relative amplitudes of the detections and the templates, are close to the expected moment magnitudes. This approach yields a source radius $r = 396$ m for the Mw3.2 mainshock with average slip $\bar{d} = 2.5$ cm. Estimates for all TM detections above M_c assuming the same $\Delta\tau$ are plotted in Fig. 8a and discussed later. Tests for different stress drops did not change the main conclusions of the exercise we are about to develop.

By taking along-strike bins with 400 m support centered at the hypocenter to group the events (i.e., a support significantly larger than the foci uncertainty), Fig. 7d shows the events cumulative count every 24 h, where the black line represents the total number of foreshocks (blue lines) and the red thick line the total number of aftershocks (red lines), all of them above M_c . Interestingly, the number of foreshocks far from the hypocenter (about 1 km) is significantly higher than in the

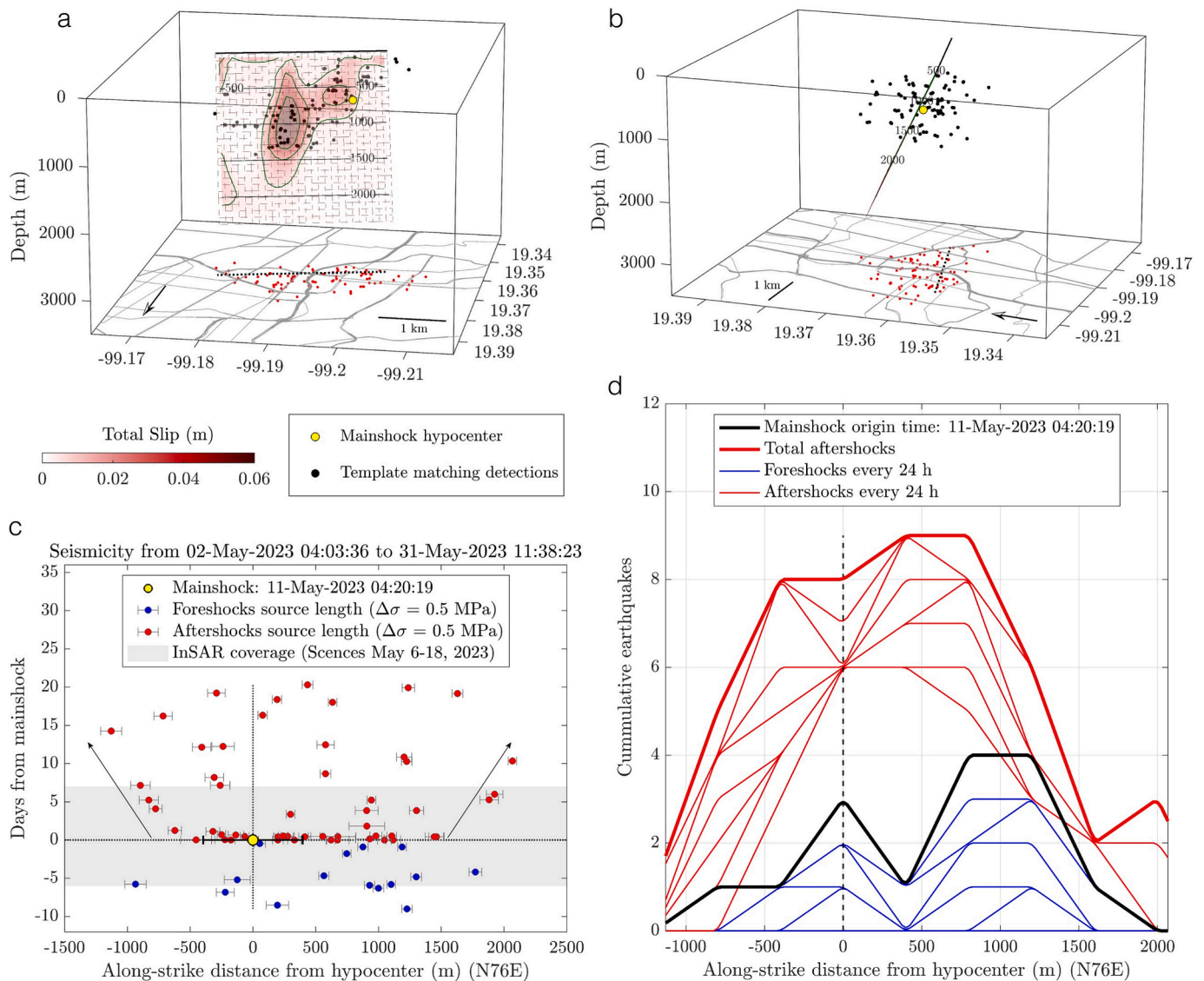


Fig. 7. Analysis of the template matching detections for May 2023. (a-b) Three-dimensional rendering of detected earthquakes around the May slip event on the Barranca del Muerto fault. The bottom gray lines depict the Mexico City main streets and the yellow dot the mainshock of May 11, 2023. (c) Fault along-strike projection of the events and their timing with respect to the mainshock of May 11 (yellow dot). Blue dots correspond to foreshocks and red dot to aftershocks. The horizontal brackets show the source length of each event estimated from Eshelby's model for a stress drop of 0.5 MPa. The gray band represents the time interval between the two InSAR scenes used to invert the slip shown in (a). (d) Along-strike cumulative count every 24 h of foreshocks (blue) and aftershocks (red) as a function of distance from the mainshock hypocenter. (For interpretation of the references to colour in this figure legend, the reader is referred to the web version of this article.)

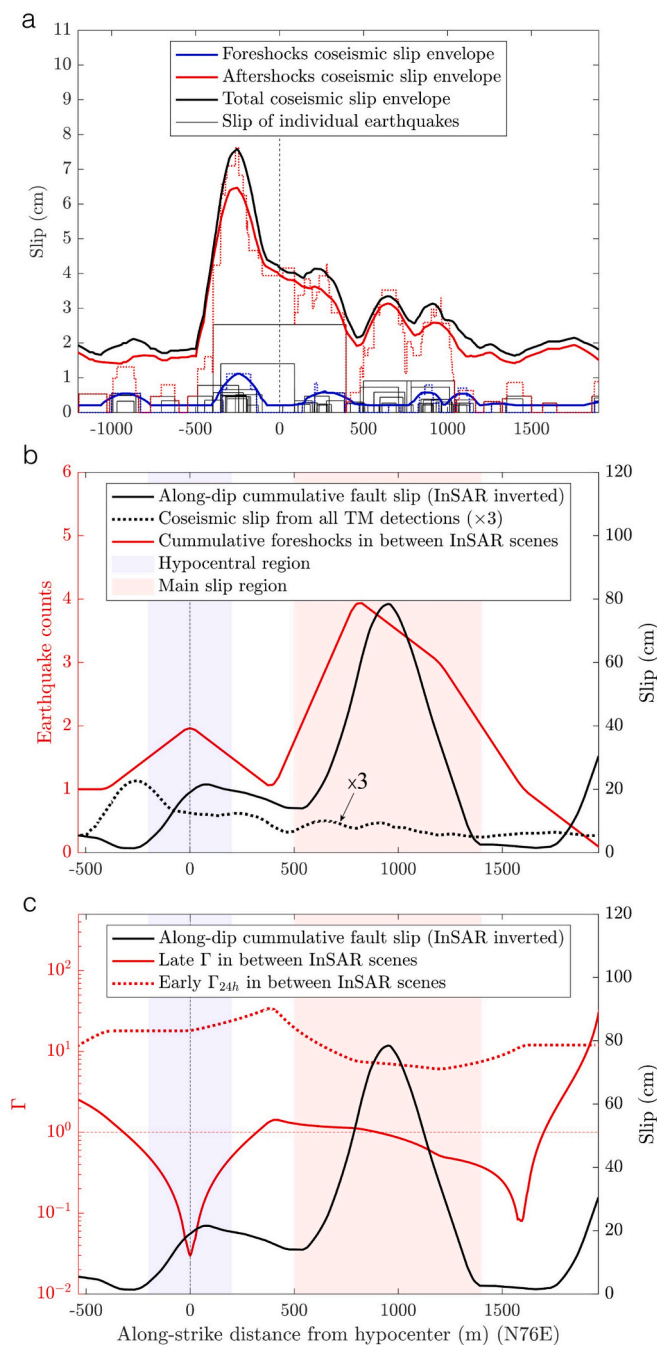


Fig. 8. Analysis of the template matching detections for May 2023. (a) Individual average slip for all detections (boxcars) estimated from Eshelby's model assuming a stress drop of 0.5 MPa as a function of the along-strike distance from the mainshock hypocenter. The blue and red curves depict the envelopes of the cumulative slip from foreshocks and aftershocks, respectively, and the black curve the cumulative slip for all the events. (b) Comparison of the cumulative count of foreshocks (red curve), the InSAR-inverted along-dip cumulative slip (black curve) on the BM fault, and the cumulative slip from all foreshocks (dotted curve) show in (a) with the blue curve. (c) Comparison between the InSAR-inverted along-dip cumulative slip (black curve) on the BM fault and the aftershocks vs. foreshocks production rates during the first 24 h after the mainshock (dotted red curve) and for the remaining five days before the second InSAR scene used to invert the slip event in the BM fault (solid red curve). See text of Section 2.5. (For interpretation of the references to colour in this figure legend, the reader is referred to the web version of this article.)

hypocentral region. The location of this seismogenic spot coincides with the slip largest, deep asperity shown in panel a, suggesting a nucleation process in that area and stress accumulation around the hypocentral area. In case that the aseismic slip preceded the mainshock, the foreshock distribution suggests that this process may have occurred deeper and ~ 1 km away. Regarding the aftershocks, three things are clear: (1) they were abundant during the first 24 h all the way from the hypocentral region to the eastern deep segment (Fig. 7d), (2) after those 24 h, their occurrence rates decrease sharply and becomes similar to those before the mainshock, and (3) about four days after the mainshock, events gradually move away from the rupture area in both opposite directions (arrows in Fig. 7c). In Fig. 8a we show the coseismic slip distribution associated with all TM detections predicted by Eshelby's model. The boxcars represent the source length and average slip of each event, while the blue and red curves depict the cumulative slip envelopes of the foreshocks and aftershocks, respectively. As expected, most of the slip comes from the aftershocks sequence. However, if we compare the total coseismic slip (black dotted curve) with the along-dip cumulative slip inverted from InSAR data (within the 1 cm slip contour, black curve) (Fig. 8b), we find that the inverted slip on the fault is much larger, 9.5 times on average, than the events coseismic slip, and 25.6 times larger in the deep slip patch 1 km east of the hypocenter. Near the hypocenter, cumulative coseismic slip from all detections above M_c including the mainshock is 3 times smaller, suggesting that the geodetically inverted slip can only be marginally explained by the sum of the co-seismic and post-seismic slip associated with the mainshock. Although the magnitude of the events on the main-slip deep region is small (and therefore have a small coseismic slip contribution; panel a), the cumulative count of foreshocks in between both InSAR scenes is the largest (more than twice as large as in the hypocentral region), as depicted by the red curve, indicating that aseismic slip could happen in this region prior to the mainshock rupture (i.e., at least during the six days preceding the earthquake).

Whether or not slow aseismic slip occurred on the fault days before the Mw3.2 earthquake (i.e., whether the InSAR inverted slip partly occurred before the mainshock) may also be assessed by comparing the foreshocks and aftershocks occurrence rates in between the two InSAR scenes (i.e., within the gray band of Fig. 7c) for events with magnitude larger than M_c . Since the aftershocks production is the largest during the first 24 h following the mainshock (Fig. 7d), we estimated the occurrence rates separately for those 24 h and then for the remaining days before the second InSAR scene. If we define the relative earthquake production rate as $\Gamma = R_a / R_f$, where R_a is the aftershocks rate and R_f is the foreshocks rate, then Fig. 8c shows that during the first 24 h (i.e., Γ_{24h}), aftershocks production was ~ 7 to ~ 30 times larger than foreshocks across the whole width of the fault (red dotted curve). Interestingly, about 1 km away from the hypocenter where the largest slip patch is found, Γ_{24h} is minimum, about 3 to 5 times smaller than in the two adjacent segments. After 24 h, a different scenario comes out with two major traits (red curve): (1) aftershocks production rate is larger than foreshocks (i.e., $\Gamma > 1$) where the InSAR inverted slip is minimum (i.e., within the white background areas), and (2) foreshocks production rate is larger than aftershocks (i.e., $\Gamma < 1$) in the hypocentral and half of the main slip segments. This means that during the six days between the first InSAR scene and the mainshock, foreshocks were highly active in both geodetic slip maxima segments (blue and red background shades) as compared with aftershocks during the last five days preceding the second InSAR scene, indicating that slow aseismic slip on both fault segments may have occurred, acting as the driving process that modulated the foreshock activity.

2.6. December event on the Mixcoac Fault

As mentioned earlier, it is unclear whether the hypocenter of the Mw3.2 earthquake of December 14 is located on the Mixcoac fault that explains the InSAR data (yellow dot Fig. 5c). Fig. 9a shows the RMS

errors for the P- and/or S-waves arrival times at 48 seismic stations with epicentral distance smaller than 10 km (Fig. 1 shows those within the study region), estimated for all possible foci locations in a 3D volume together with our preferred hypocentral location (gray star). Overall errors smaller than 0.2 s enclose the western half of the fault where the western slip asperity is located (Figs. 4d and 5c) and thus where the mainshock hypocenter is likely found. However, as expected, the RMS resolution is poorer in depth. We thus analyzed the characteristics of that asperity and confront them with theoretical predictions for an Mw3.2 rupture. The Eshelby's (1957) source model introduced in the previous section predicts the slip distribution within a circular crack with radius r and stress drop $\Delta\tau$. By centering the source in the asperity, a grid search for both parameters to minimize the mean absolute error between the model and the inverted slip yields optimal values $r = 320$ m and $\Delta\tau = 1.05$ MPa for a mean slip $\bar{d} = 4.3$ cm. Both slip distributions are shown in Fig. 9b, where we also report the resulting magnitude $M_w = 3.2$ for the optimal Eshelby's model, which is consistent with the earthquake's magnitude. Nonetheless, considering that the inverted slip

has uncertainties (particularly along-dip as shown by the MOC test, Fig. S10) and includes also the postseismic relaxation of the event, the asperity model should be biased to some extent. This could explain the relatively high stress drop found, which is twice as large as determined for the Mw3.2 earthquake of May 11 (Quintanar et al., 2024). If we assume an afterslip of 20%, the Eshelby's model predicts $\Delta\tau = 0.84$ MPa with $M_w = 3.17$, which is probably closer to the coseismic signature of the earthquake. From these exercises we conclude that the western slip patch may indeed correspond to the December 14 earthquake rupture.

The analysis above suggests that large part of the InSAR-inverted slip (i.e., the slip outside the mainshock asperity located in the western portion of the fault) was released aseismically. Since relocated seismicity for December (dark blue dots in Fig. 4c) is away from the fault, a similar TM analysis as for the May event to draw a timeline of the slip history becomes difficult. We do have, though, two interferograms for December (inverted simultaneously) with initial scenes taken 6 and 3 days before the mainshock, which could in principle be analyzed separately to identify whether there was activity on the fault in the non-

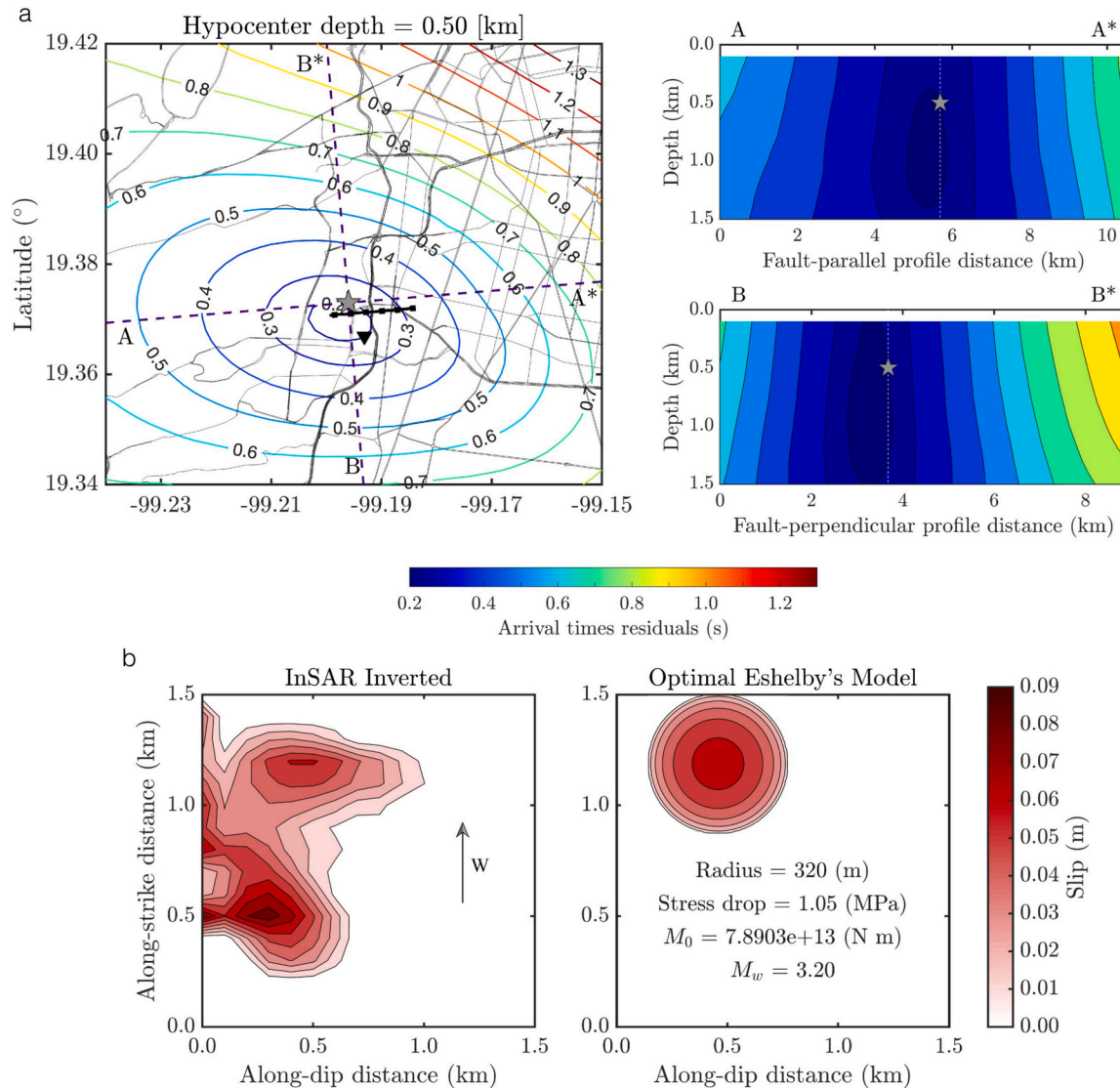


Fig. 9. (a) RMS errors for the P- and/or S-waves arrival times at 48 seismic stations with epicentral distance smaller than 10 km, estimated for all possible foci locations in a 3D volume together with our preferred hypocentral location for the December 14, 2023, mainshock (gray star). (b) Comparison between the InSAR inverted slip for the December event on the Mixcoac fault (left) and the slip distribution that best explains the western slip asperity (right) given by the Eshelby model. The optimal model parameters are given within the right panel.

overlapping period. However, as discussed in detail on Section 2.2, there was no significant deformation between December 8 and December 11, the initial dates of the two interferograms (Fig. S2). Therefore, the slip east of the fault must have occurred between December 11 and December 23. That is, in the three days prior to the mainshock or later. A smaller (but significant) earthquake than the Mw3.2 of December 14 occurred on December 12 with moment magnitude $M_w = 3.0$ (Bello et al., personal communication, 2024). Yet, our double-difference hypocentral relocation is 600 m west of the fault (Fig. 4d), so the possibility that the eastern slip asperity could correspond to the coseismic signature of that foreshock is unlikely. The most reasonable hypothesis is, therefore, that the slip east of the fault was slow slip and thus aseismic. There are two possibilities. Either it occurred in the three days prior to the mainshock, as seems to have occurred before the May mainshock in the BM fault, or afterwards, as an extended along-strike afterslip.

2.7. Fault interaction

Whether or not the above hypothesis is true, one wonders how the May slip on the BM fault could have affected the strain field around the Mixcoac fault, which was activated in December only 800 m to the north (see Fig. 5c). Fig. 10 shows a 3D rendering of the Coulomb Failure Stress (CFS) change, estimated with an artifact-free triangular dislocation model (Nikkhoo and Walter, 2015), imparted by the May event on the Mixcoac fault, where we also include the slip contours of our joint inversion, shown in Figs. 4d and 9b. Two main features stand out: (1) the CFS features a large negative patch below ~ 700 m, with minimum values reaching -40 kPa at ~ 1.2 km depth, where no slip for the December event is found, and (2) the CFS is positive and maximum, with values above 10 kPa, in the eastern shallow segment where the main slip asperity is found. This means that the May event on the BM fault may have inhibited deep slip on the Mixcoac fault and promoted slip on its shallow part, particularly to the east, which may explain why slip concentrated near the surface unlike the May event. Although the prestress condition on the Mixcoac fault is unknown, it is striking how the slip distribution, which most likely includes the coseismic signature of the December 14 mainshock, seems to surround the deep stress shadow. Thus, the stress interaction between the two faults indeed supports the evidence discussed in the previous paragraph, which points to the occurrence of shallow aseismic slow slip about 600 m east of where the mainshock happened.

3. Discussion

3.1. Origin of Slow Slip Beneath Mexico City

Although local seismic swarms are likely to be formed by small ruptures across an extended fault system, temporal clustering of the events should be driven by local underlying processes, as happens with the induced seismicity during borehole injection tests. In these cases, there is growing evidence that fluid diffusion induces changes in the pore pressure that stabilize friction and leads to aseismic slip instabilities that trigger seismic radiation in the fault system (Cappa et al., 2019; Guglielmi et al., 2015; Larochelle et al., 2021; Wang and Dunham, 2022). Fault system pressurization can also produce surface deformations measurable with satellite interferometry in sedimentary basins such as the Delaware, USA, where deformations are due to slip on shallow normal faults around which most of the seismicity takes place (Pepin et al., 2022). This case seems to be an analogy of what is happening in the Valley of Mexico basin, where uninterrupted groundwater extraction produces one of the highest subsidence rates in the world (i.e., up to 500 mm/yr) (Cabral-Cano et al., 2008; Chaussard et al., 2021; López-Quiroz et al., 2009; Ortega-Guerrero et al., 1999). The buried segments of the BM and Mixcoac faults are in a very densely populated area where water demand is high and some 14 wells are located within 1 km of the faults (Júnez-Ferreira et al., 2023). The high foreshocks rate in both the deepest segment of the BM fault and the shallow hypocentral zone of the Mw3.2 mainshock (Figs. 7d and 8c) strongly suggests that part of the surface deformation in May occurred before the earthquake due to aseismic slip primarily in the deeper fault area, located ~ 1 km east the hypocenter. The scalar moment of the slip events on both faults (Fig. 4) are 22 and 11 times larger than those of the associated Mw3.2 mainshocks. On the BM fault, where the largest and deepest slip occurred, only 5 % of the inverted slip can be explained coseismically from our seismic catalog with completeness magnitude 1.2. This means that 95 % of the May slip was aseismic, which is close to the 98 % found in the Delaware basin (Pepin et al., 2022). On the Mixcoac fault, from Fig. 9b we can estimate that about 70 % of the seismic moment was released aseismically in December, a percentage consistent with estimates made in Nevada, USA, and the Apennines, Italy, from geodetic deformations associated with seismic swarms in the absence of water injection (Gualandi et al., 2017; Jiang et al., 2022). While this slow slip could be partly attributed to underground fluid diffusion, as has been demonstrated on natural faults, in the laboratory,

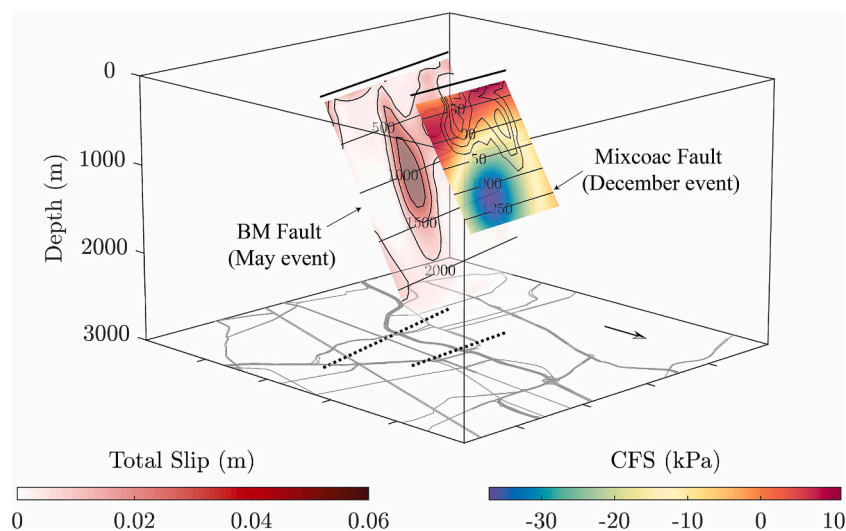


Fig. 10. Coulomb Failure Stress (CFS) change imparted by the May slip event on the Mixcoac fault. Black contours on the Mixcoac fault correspond to the inverted slip for the December event shown in Figs. 4d. Notice how the shallow slip distribution on the Mixcoac fault surrounds the deep stress shadow and concentrates to the east, where CFS is maximum.

and with sophisticated friction models (Cappa et al., 2019; Guglielmi et al., 2015; Laroche et al., 2021; Wang and Dunham, 2022), unlike controlled water injection, extraction in Mexico City is sustained over time, making it difficult to attribute the slip events and associated seismicity to particular time-bound anthropogenic incidents.

Earthquakes between December 2023 and May 2024 concentrate west and southwest of the Mixcoac fault (Fig. 4d) as do most of the events reported by the SSN in 2023. That is, mainly in the hilly area west of the city where the faults are expressed geomorphologically (Figs. 1 and 5). Furthermore, the distribution of seismicity following the May 11 and December 14 mainshocks moves away from the slip zones with time, as can be seen in Fig. 7c (black arrows) on the BM fault and in Fig. 4d (compare dark blue dots with light blue dots) around the Mixcoac fault. Also striking is the absence of seismicity on the Mixcoac fault before and after the mainshock. These seismicity patterns suggest that the eastern flanks of both faults are prone to slow aseismic slip unlike their westward extensions, where the faults emerge at surface. The largest slip occurred on buried fault segments below the flat part of the basin where the soil is composed of water-rich alluvial deposits and clays. The nature of aseismic slip under similar basin conditions depends on the hydraulic permeability of the medium, the fault prestress and its constitutive friction parameters, so that slow slip propagation is mainly driven by changes in pore pressure and the subsequent drop in fault strength. This mechanism explains the migration of seismicity in the Cooper basin, New Zealand (Wang and Dunham, 2022), and may explain the outward migration of microseismicity near the slip zone, especially on the BM

fault (Fig. 7c).

3.2. Fault system mechanical transition and intense seismicity

The more general seismicity pattern can be explained by a similar but different mechanism also suggested by our results. The aseismic slip on fault segments buried beneath sediments with high water content and the concentration of intense seismicity to the west where the faults have a geomorphic expression (i.e., where sediments are relatively scarce) suggest that the dynamic instabilities causing the seismicity are partly due to stress loading to the west induced by aseismic slip on the buried segments. That is, the fault system west of Mexico City could be divided into two mechanically differentiated zones with a transition in between (Fig. 11). On one hand, a dominant eastern regime of stable slow slip in the buried segments beneath the sediments, and another of unstable seismic slip to the west, beneath the hilly zone of the city. Complementary evidence for this conjecture is the absence of intense seismicity in the vicinity of the Mixcoac fault during the December event, and the location of the two Mw3.2 mainshocks of May and December near the western ends of the faults (Figs. 4 and 5a), and thus where the stress loading should be high near the mechanical transition of the fault system from stable to unstable slip (Fig. 11). A similar conclusion was reached after studying hydraulic fracturing-induced seismicity in different locations around the world, where pore pressure-driven aseismic slip activates unstable slip (i.e., intense seismic radiation) along distal nonpressurized fault segments (Eyre et al., 2019, 2022).

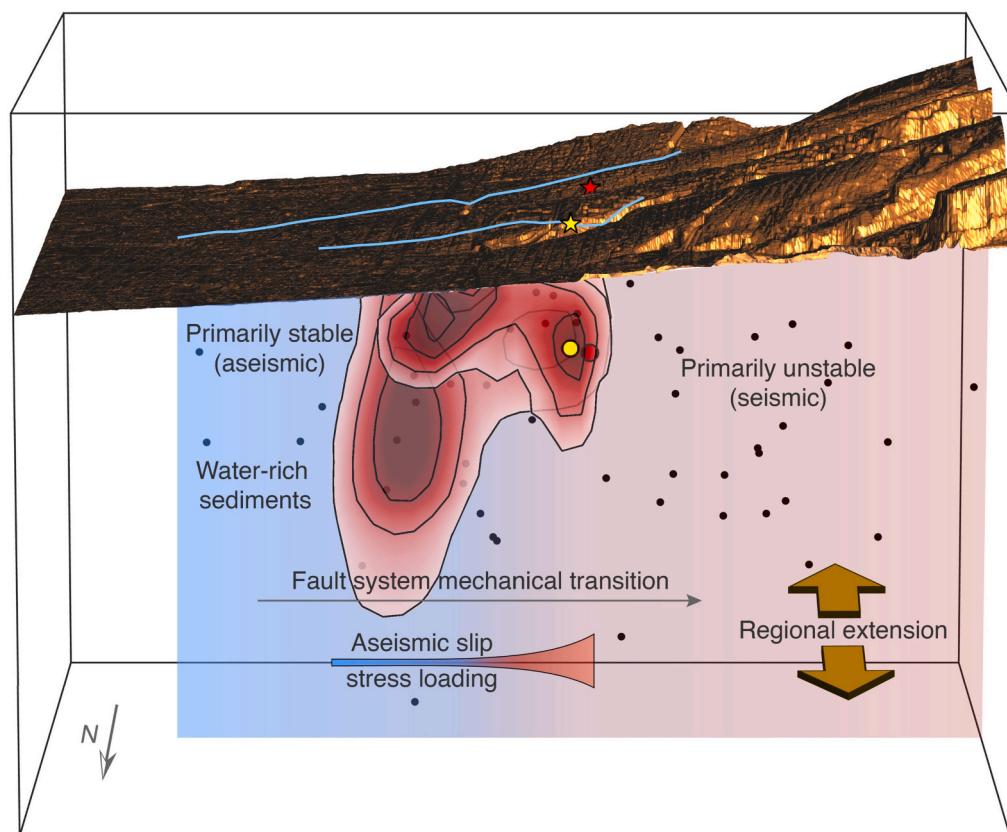


Fig. 11. Conceptual model summarizing the main findings and ideas. Major aseismic slip asperities to the east of both faults (see Fig. 4) produce stress buildup to the west, where the most intense 2023–2024 microearthquakes are concentrated. Slow slip occurs on the flat part of the city beneath water-rich sediments promoting aseismic deformations. The earthquakes shown (black dots) correspond to the double-difference relocations reported in Fig. 4a and d and arise from an extended fracture system where the major faults have a geomorphic expression west of the city. Note that the two Mw3.2 mainshocks of May 11 (red symbols) and December 14 (yellow symbols) are located near the western ends of the slip faults, where a mechanical transition between stable and unstable slip appears to occur. The studied seismic swarms may thus be a consequence of the regional N-S extensional regime, the stresses induced by slow slip on the eastern fault segments, and the elastic interaction between these major faults. (For interpretation of the references to colour in this figure legend, the reader is referred to the web version of this article.)

3.3. Seismic Hazard Associated with the BM and Mixcoac Faults

To our knowledge, this is the first three-dimensional mapping of seismogenic faults in Mexico City (see geological compilation by Arce et al., 2019). Their extent invites thinking about the seismic potential they could pose, a particularly sensitive issue in one of the most populated cities in the world. Assuming that both faults could produce earthquakes with moment magnitude similar to those of the inverted slip (i.e., \sim Mw4.0) would seem unrealistic, at least in the buried segments of the faults, where deformation seems to be preferentially accommodated aseismically. In other words, presuming that the fault extent determines the maximum magnitude of an earthquake means disregarding what the international community has understood about the dynamic rupture mechanics of faults in the light of slow slip events. In a recent study, Singh et al. (2020) postulated a Mw5.0 scenario for Mexico City based on the records of a nearby and similar earthquake (Mw3.2) on July 2019 (Fig. 1) that produced the largest peak ground acceleration (PGA) ever recorded in the bedrock of the city, with 213 gal in geometric average of the three components (i.e., 7.4 and 4.4 times larger than those recorded in bedrock during the devastating earthquakes of 1985 and 2017, respectively; see Singh et al., 2018). These authors then postulated a hypothetical rupture 3 to 4 km in extent, which would be consistent with the 3.5 to 4.5 km length of the geomorphologic expressions of the BM and Mixcoac faults (dashed gray lines in Fig. 1). The estimated response spectra for such a scenario at a site upon lake-bed soft deposits of the basin (i.e., 7.3 km east of the 2019 epicenter) are smaller (roughly by a factor of 2 up to 5 s period) than those recorded nearby during the devastating 1985 and 2017 earthquakes. However, these estimates are valid in the far field and for a point source. In other words, the extended rupture of a \sim Mw5.0 earthquake west of the city could imply a different scenario close to the source (i.e., at distances on the order of \sim 5 km), with significant damage due to the rupture propagation and its near-field effects that, combined with the three-dimensional propagation of waves in a basin with exceptionally extreme properties (Chávez-García and Bard, 1994; Cruz-Atienza et al., 2016; Hernández-Aguirre et al., 2023), could produce ground motions not yet observed in Mexico City, as unexpectedly occurred during the 1985 and 2017 earthquakes despite the knowledge gathered by experts up to those two dramatic moments in history.

4. Conclusions

In this investigation we have studied the 2023–2024 seismic crisis in Mexico City from a broad perspective. Tectonically driven satellite observations in a densely populated area west of the city allowed us to identify two east-west trending normal faults as responsible for the deformations. The first slip event occurred on the BM fault during the days before and after the Mw3.2 mainshock on May 11, 2023, and whose coseismic signature is located 1 km west of the main slip patch with depth \sim 1.2 km. The second event occurred on the Mixcoac fault, 800 m to the north, with shallower slip likely reaching the surface (i.e., above \sim 600 m mostly) and coincident with another Mw3.2 mainshock on December 14, 2023. A detailed microseismicity analysis revealed that more than 95 % of the slip on the BM fault was aseismic and initiated at least 6 days before the May 11 earthquake in the slip patch distant from the hypocenter. For the December event on the Mixcoac fault, approximately 70 % of the slip was aseismic. Stresses induced on the Mixcoac fault by May slip on the BM fault could explain why the December slip was shallow and concentrated east of the December 14 hypocenter. A quantitative geomorphological analysis of the surrounding hillsides indicates that the preferential direction of their north-facing slopes is consistent with the dip directions of both faults. This, together with the alignment of the faults with two gullies to the west, allowed establishing the structural connection between the buried faults to the east and their geomorphic expression to the west with extensions of 3.5 and 4.5 km, which are consistent with the rupture of a hypothetical Mw5.0 earthquake

proposed in recent literature. The seismicity patterns analyzed and the dominant aseismic slip on the faults suggest that the seismotectonics of western Mexico City can be divided into two mechanically distinct regions. A stable region prone to aseismic deformation to the east where faults are buried under sediments with high water content, and an unstable region to the west, prone to seismic radiation where faults are expressed geomorphologically. Therefore, the earthquake swarms characterizing the western part of Mexico City seem to be a consequence of the regional extensional regime, the stresses induced by slow earthquakes in the eastern segments of the faults and the elastic interaction between these main faults.

Supplementary data to this article can be found online at <https://doi.org/10.1016/j.tecto.2025.230659>.

CRediT authorship contribution statement

Manuel J. Aguilar-Velázquez: Conceptualization, Methodology, Software, Formal analysis, Investigation, Data curation, Writing – original draft, Visualization, Writing – review & editing. **Paulina Miranda-García:** Software, Investigation, Data curation, Visualization, Writing – review & editing. **Victor M. Cruz-Atienza:** Conceptualization, Methodology, Software, Validation, Formal analysis, Investigation, Data curation, Writing – original draft, Visualization, Supervision, Project administration, Writing – review & editing. **Darío Solano-Rojas:** Conceptualization, Methodology, Validation, Formal analysis, Investigation, Data curation, Writing – original draft, Visualization, Supervision, Project administration, Writing – review & editing. **Josué Tago:** Conceptualization, Methodology, Software, Validation, Data curation, Supervision, Writing – review & editing. **Luis A. Domínguez:** Methodology, Software, Formal analysis, Investigation, Data curation, Writing – original draft, Writing – review & editing. **Carlos Villafuerte:** Formal analysis, Investigation, Writing – review & editing. **Victor H. Espíndola:** Investigation, Writing – review & editing. **Delia Bello-Segura:** Investigation, Data curation, Writing – review & editing. **Luis Quintanar-Robles:** Investigation, Data curation, Writing – review & editing. **Mathieu Pertont:** Validation, Writing – review & editing.

Declaration of competing interest

The authors declare that they have no known competing financial interests or personal relationships that could have appeared to influence the work reported in this paper.

Acknowledgements

We thank Enrique González-Torres, Javier Mancera-Alejandre, Ricardo Padilla, and Guillermo Pérez-Cruz for their insights on the structural and subsurface geology of Mexico City. We also thank Graciela Herrera and Mario Hernández-Hernández for their enriching and promising discussions related to groundwater in Mexico City. This research was possible thanks to UNAM's DGPA-PAPIIT grants IN111524, IN116423, and IA105921, as well as grant LANCAD-UNAM-DGTIC-380. SSN data were obtained by the Servicio Sismológico Nacional (Mexico); station maintenance, data acquisition, and distribution are possible thanks to its personnel.

Data availability

Data will be made available on request.

References

- Aguilar-Velázquez, M.J., Pérez-Campos, X., Pita-Sllim, O., 2023. Crustal Structure Beneath Mexico City From Joint Inversion of Receiver Functions and Dispersion Curves. *J. Geophys. Res. Solid Earth* 128 (8). <https://doi.org/10.1029/2022JB025047> e2022JB025047.

- Aguilar-Velázquez, M. J., Pérez-Campos, X., Tago, J., & Villafuerte, C. (2024). Azimuthal crustal variations and their implications on the seismic impulse response in the Valley of Mexico. *Acta Geophysica*, 1–18. doi:<https://doi.org/10.1007/S11600-024-01383-7>.
- Aguirre, J., Castelán, G., Cruz-Atienza, V., Espinosa, J.M., Gómez, A., Pérez-Campos, X., et al., 2021. Red Sísmica de la Ciudad de México. *Revista de La Academia Mexicana de Ciencias* 72 (1), 60–67.
- Arce, J.L., Layer, P., Martínez, I., Salinas, J.I., Del, M., Macías-Romo, C., et al., 2015. Geology and stratigraphy in the San Lorenzo Tezonco deep well and its vicinities, southern Mexico basin. *Bol. Soc. Geol. Mex.* 67 (2), 123–143. Retrieved from. http://www.scielo.org.mx/scielo.php?script=sci_arttext&pid=S1405-33222015000200002&lng=es&nrm=iso&tng=es.
- Arce, J.L., Layer, P.W., Macías, J.L., Morales-Casique, E., García-Palomo, A., Jiménez-Domínguez, F.J., et al., 2019. Geology and stratigraphy of the Mexico Basin (Mexico City), central Trans-Mexican Volcanic Belt. *J. Maps* 15 (2), 320–332. <https://doi.org/10.1080/17445647.2019.1593251>.
- Bayona, J., Suárez, G., Ordaz, M., 2017. A probabilistic seismic hazard assessment of the Trans-Mexican Volcanic Belt, Mexico based on historical and instrumentally recorded seismicity. *Geofis. Int.* 56 (1), 87–101. <https://doi.org/10.19155/GEOFINT.2017.056.1.7>.
- Cabral-Cano, E., Dixon, T.H., Miralles-Wilhelm, F., Díaz-Molina, O., Sánchez-Zamora, O., Carande, R.E., 2008. Space geodetic imaging of rapid ground subsidence in Mexico City. *Bull. Geol. Soc. Am.* 120 (11–12), 1556–1566. <https://doi.org/10.1130/B26001.1>.
- Cappa, F., Scuderi, M.M., Collettini, C., Guglielmi, Y., Avouac, J.P., 2019. Stabilization of fault slip by fluid injection in the laboratory and in situ. *Sci. Adv.* 5 (3), eau04065. <https://doi.org/10.1126/sciadv.aau4065>.
- Chaussard, E., Havazli, E., Fattahi, H., Cabral-Cano, E., Solano-Rojas, D., 2021. Over a Century of Sinking in Mexico City: No Hope for Significant Elevation and Storage Capacity Recovery. *J. Geophys. Res. Solid Earth* 126 (4). <https://doi.org/10.1029/2020JB020648> e2020JB020648.
- Chávez-García, F.J., Bard, P.Y., 1994. Site effects in Mexico City eight years after the September 1985 Michoacán earthquakes. *Soil Dyn. Earthq. Eng.* 13 (4), 229–247. [https://doi.org/10.1016/0267-7261\(94\)90028-0](https://doi.org/10.1016/0267-7261(94)90028-0).
- Corana, A., Marchesi, M., Martini, C., Ridella, S., 1987. Minimizing multimodal functions of continuous variables with the “simulated annealing” algorithm—Corrigenda for this article is available here. *ACM Transact. Math. Software (TOMS)* 13 (3), 262–280. <https://doi.org/10.1145/29380.29864>.
- Córdoba-Montiel, F.C.-M., Krishna Singh, S., Iglesias, A., Pérez-Campos, X., Sieron, K., 2018. Estimation of ground motion in Xalapa, Veracruz, Mexico during the 1920 (M=6.4) crustal earthquake, and some significant intraslab earthquakes of the last century. *Geofis. Int.* 57 (2). <https://doi.org/10.22201/igeof.00167169p.2018.57.2.2039>.
- Cruz-Atienza, V.M., Iglesias, A., Pacheco, J.F., Shapiro, N.M., Singh, S.K., 2010. Crustal Structure below the Valley of Mexico Estimated from Receiver Functions. *Bull. Seismol. Soc. Am.* 100 (6), 3304–3311. <https://doi.org/10.1785/0120100051>.
- Cruz-Atienza, V.M., Tago, J., Sanabria-Gómez, J.D., Chaljub, E., Etienne, V., Virieux, J., Quintanar, L., 2016. Long Duration of Ground Motion in the Paradigmatic Valley of Mexico. *Sci. Rep.* 6 (1), 1–9. <https://doi.org/10.1038/srep38807>.
- Elliott, J.R., Walters, R.J., Wright, T.J., 2016. The role of space-based observation in understanding and responding to active tectonics and earthquakes. *Nat. Commun.* 7 (1), 1–16. <https://doi.org/10.1038/ncomms13844>.
- Eyre, T.S., Eaton, D.W., Garagash, D.I., Zecевич, M., Venieri, M., Weir, R., Lawton, D.C., 2019. The role of aseismic slip in hydraulic fracturing-induced seismicity. *Sci. Adv.* 5 (8). <https://doi.org/10.1126/SCIADV.AAV7172>.
- Eyre, T.S., Samsonov, S., Feng, W., Kao, H., Eaton, D.W., 2022. InSAR data reveal that the largest hydraulic fracturing-induced earthquake in Canada, to date, is a slow-slip event. *Sci. Rep.* 12 (1), 1–12. <https://doi.org/10.1038/s41598-022-06129-3>.
- Farr, T.G., Rosen, P.A., Caro, E., Crippen, R., Duren, R., Hensley, S., et al., 2007. The Shuttle Radar Topography Mission. *Rev. Geophys.* 45 (2), 2004. <https://doi.org/10.1029/2005RG000183>.
- Ferrari, L., Orozco-Esquivel, T., Manea, V., Manea, M., 2012. The dynamic history of the Trans-Mexican Volcanic Belt and the Mexico subduction zone. *Tectonophysics* 522, 122–149. <https://doi.org/10.1016/j.tecto.2011.09.018>.
- Figuerola, J., 1971. Sismicidad en la Cuenca del Valle de México, Serie de Investigación. Serie de Investigación. Instituto de Ingeniería, UNAM, Mexico City, Mexico, p. 289.
- Flores, T., Camacho, H., 1922. Memoria relativa al terremoto mexicano del 3 de enero de 1920. *Boletín Del Instituto Geológico de México* 38.
- Foulger, G.R., Wilson, M.P., Gluyas, J.G., Julian, B.R., Davies, R.J., 2018. Global review of human-induced earthquakes. *Earth Sci. Rev.* 178, 438–514. <https://doi.org/10.1016/J.EARSCIREV.2017.07.008>.
- Ge, S., Saar, M.O., 2022. Review: Induced Seismicity During Geoenery Development—A Hydromechanical Perspective. *J. Geophys. Res. Solid Earth* 127 (3). <https://doi.org/10.1029/2021JB023141> e2021JB023141.
- GRASS Development Team, 2022. GRASS GIS (7.8.7).
- Gualandi, A., Nichele, C., Serpelloni, E., Chiaraluce, L., Anderlini, L., Latorre, D., et al., 2017. Aseismic deformation associated with an earthquake swarm in the northern Apennines (Italy). *Geophys. Res. Lett.* 44 (15), 7706–7714. <https://doi.org/10.1002/2017GL073687>.
- Guglielmi, Y., Cappa, F., Avouac, J.P., Henry, P., Elsworth, D., 2015. Seismicity triggered by fluid injection-induced aseismic slip. *Science* 348 (6240), 1224–1226. <https://doi.org/10.1126/science.aab0476>.
- Havskov, J., 1982. The earthquake swarm of february 1981 in Mexico City. *Geofis. Int.* 21 (2), 157–175. <https://doi.org/10.22201/IGEOF.00167169P.1982.21.2.909>.
- Hernández-Aguirre, V. M., Paolucci, R., Sánchez-Sesma, F. J., & Mazzieri, I. (2023). Three-dimensional numerical modeling of ground motion in the Valley of Mexico: A case study from the Mw3.2 earthquake of July 17, 2019. <https://doi.org/10.1177/87552930231192463>, 39(4), 2323–2351. doi:<https://doi.org/10.1177/87552930231192463>.
- Instituto Nacional de Estadística y Geografía, INEGI, 2024. Modelos Digitales de Elevación de Alta Resolución LiDAR E14A39B3, con resolución de 5 m. Superficie. Retrieved June 26, 2024, from. <https://www.inegi.mx/temas/relieve/continental/#Descargas>.
- Jasiewicz, J., Stepinski, T.F., 2013. Geomorphons — a pattern recognition approach to classification and mapping of landforms. *Geomorphology* 182, 147–156. <https://doi.org/10.1016/J.GEOMORPH.2012.11.005>.
- Jiang, G., Wen, Y., Liu, Y., Xu, X., Fang, L., Chen, G., et al., 2015. Joint analysis of the 2014 Kangding, southwest China, earthquake sequence with seismicity relocation and InSAR inversion. *Geophys. Res. Lett.* 42 (9), 3273–3281. <https://doi.org/10.1002/2015GL063750>.
- Jiang, Y., Samsonov, S.V., González, P.J., 2022. Aseismic Fault Slip During a Shallow Normal-Faulting Seismic Swarm Constrained Using a Physically Informed Geodetic Inversion Method. *J. Geophys. Res. Solid Earth* 127 (7). <https://doi.org/10.1029/2021JB022621> e2021JB022621.
- Júnez-Ferreira, H.E., Hernández-Hernández, M.A., Herrera, G.S., González-Trinidad, J., Cappello, C., Maggio, S., De Iaco, S., 2023. Assessment of changes in regional groundwater levels through spatio-temporal kriging: application to the southern Basin of Mexico aquifer system. *Hydrogeol. J.* 31 (6), 1405–1423. <https://doi.org/10.1007/S10040-023-02681-Y/FIGURES/13>.
- Khorrami, M., Shirzaei, M., Ghobadi-Far, K., Werth, S., Carlson, G., Zhai, G., 2023. Groundwater Volume Loss in Mexico City Constrained by InSAR and GRACE Observations and Mechanical Models. *Geophys. Res. Lett.* 50 (5). <https://doi.org/10.1029/2022GL101962> e2022GL101962.
- Lacan, P., Arango-Galván, C., Lacan, P., Arango-Galván, C., 2021. Geophysical evidence of the 1912 earthquake rupture along the central fault system of the Acambay Graben, Central Mexico. *Bol. Soc. Geol. Mex.* 73 (2), 1–19. <https://doi.org/10.18268/BSGM2021V73N2A250121>.
- Larochelle, S., Lapusta, N., Ampuero, J.P., Cappa, F., 2021. Constraining fault friction and stability with fluid-injection field experiments. *Geophys. Res. Lett.* 48 (10). <https://doi.org/10.1029/2020gl091188> e2020GL091188.
- León-Loya, R., Lacan, P., Ortuño, M., Zúñiga, F.R., Stépánčíková, P., Stemberk, J., et al., 2023. Paleoseismology of a Major Crustal Seismogenic Source Near Mexico City: The Southern Border of the Acambay Graben. *Tectonics* 42 (6). <https://doi.org/10.1029/2022TC007610> e2022TC007610.
- Lermo, J., Santoyo, M.A., Jaimes, M.A., Antayhua, Y., Chavacán, M., 2016. Local Earthquakes of the Mexico Basin in Mexico City: κ , Q, Source Spectra, and Stress Drop. *Bull. Seismol. Soc. Am.* 106 (4), 1423–1437. <https://doi.org/10.1785/0120150189>.
- Liu, M., Li, H., Zhang, M., Wang, T., 2020. Graphics Processing Unit-Based Match and Locate (GPU-M&L): An Improved Match and Locate Method and Its Application. *Seismol. Res. Lett.* 91 (2A), 1019–1029. <https://doi.org/10.1785/0220190241>.
- Lohman, R.B., McGuire, J.J., 2007. Earthquake swarms driven by aseismic creep in the Salton Trough, California. *J. Geophys. Res. Solid Earth* 112 (B4). <https://doi.org/10.1029/2006JB004596>.
- Lohman, Rowena B., Simons, M., 2005. Some thoughts on the use of InSAR data to constrain models of surface deformation: Noise structure and data downsampling. *Geochem. Geophys. Geosyst.* 6 (1). <https://doi.org/10.1029/2004GC000841>.
- López-Quiroz, P., Doín, M.P., Tupin, F., Briole, P., Nicolas, J.M., 2009. Time series analysis of Mexico City subsidence constrained by radar interferometry. *J. Appl. Geophys.* 69 (1), 1–15. <https://doi.org/10.1016/J.JAPGEO.2009.02.006>.
- Manzanilla, L., 1986. Relación de los sismos ocurridos en la ciudad de México y sus efectos. *Rev. Mex. Sociol.* 48 (2), 265. <https://doi.org/10.2307/3540365>.
- Mirwald, A., Cruz-Atienza, V.M., Díaz-Mojica, J., Iglesias, A., Singh, S.K., Villafuerte, C., Tago, J., 2019. The 19 September 2017 (Mw7.1) Intermediate-Depth Mexican Earthquake: A Slow and Energetically Inefficient Deadly Shock. *Geophys. Res. Lett.* 46 (4). <https://doi.org/10.1029/2018GL080904>.
- Moein, M.J.A., Langenbruch, C., Schultz, R., Grigoli, F., Ellsworth, W.L., Wang, R., et al., 2023. The physical mechanisms of induced earthquakes. *Nat. Rev. Earth Environ.* 4 (12), 847–863. <https://doi.org/10.1038/s43017-023-00497-8>.
- Mooser, F., 1972. The Mexican Volcanic Belt structure and tectonics. *Geofis. Int.* 12 (2), 55–70. <https://doi.org/10.22201/IGEOF.00167169P.1972.12.2.1024>.
- Nikkhoo, M., Walter, T.R., 2015. Triangular dislocation: an analytical, artefact-free solution. *Geophys. J. Int.* 201 (2), 1119–1141. <https://doi.org/10.1093/GJI/GGV035>.
- Okada, Y., 1985. Surface deformation due to shear and tensile faults in a half-space. *Bull. Seismol. Soc. Am.* 75 (4), 1135–1154. <https://doi.org/10.1785/BSSA0750041135>.
- Ordaz, M., Singh, S.K., 1992. Source spectra and spectral attenuation of seismic waves from Mexican earthquakes, and evidence of amplification in the hill zone of Mexico City. *Bull. Seismol. Soc. Am.* 82 (1), 24–43. <https://doi.org/10.1785/BSSA0820010024>.
- Ortega-Guerrero, A., Rudolph, D.L., Cherry, J.A., 1999. Analysis of long-term land subsidence near Mexico City: Field investigations and predictive modeling. *Water Resour. Res.* 35 (11), 3327–3341. <https://doi.org/10.1029/1999WR900148>.
- Osmanoğlu, B., Dixon, T.H., Wdowinski, S., Cabral-Cano, E., Jiang, Y., 2011. Mexico City subsidence observed with persistent scatterer InSAR. *Int. J. Appl. Earth Obs. Geoinf.* 13 (1), 1–12. <https://doi.org/10.1016/J.JAG.2010.05.009>.
- Pepin, K.S., Ellsworth, W.L., Sheng, Y., Zebker, H.A., 2022. Shallow Aseismic Slip in the Delaware Basin Determined by Sentinel-1 InSAR. *J. Geophys. Res. Solid Earth* 127 (2). <https://doi.org/10.1029/2021JB023157>.
- QGIS Project, 2024. QGIS 3.12.1. Retrieved from. <https://qgis.org>.
- Quintanar, Luis, Cárdenas-Ramírez, A., Bello-Segura, D.I., Espíndola, V.H., Pérez-Santana, J.A., Cárdenas-Monroy, C., et al., 2018. A Seismic Network for the Valley of

- Mexico: Present Status and Perspectives. *Seismol. Res. Lett.* 89 (2A), 356–362. <https://doi.org/10.1785/0220170198>.
- Quintanar, L., Singh, S. K., Espíndola, V. H., Iglesias, A., Bello-Segura, D., Arroyo, D., et al. (2024). Mexico City Earthquake of 11 May 2023 (Mw3.2). *Geofis. Int.*, 63(2), 749–762. doi:10.22201/IGEOF.2954436XE.2024.63.2.1757.
- Reinoso, E., Ordaz, M., 1999. Spectral Ratios for Mexico City from Free-Field Recordings. *Earthquake Spectra* 15 (2), 273–295. <https://doi.org/10.1193/1.1586041>.
- Segall, P., 1989. Earthquakes triggered by fluid extraction. *Geology* 17 (10), 942–946. Retrieved from. <https://pubs.geoscienceworld.org/gsa/geology/article-abstract/17/10/942/186508/Earthquakes-triggered-by-fluid-extraction>.
- Singh, S.K., Mena, E., Castro, R., 1988. Some aspects of source characteristics of the 19 September 1985 Michoacan earthquake and ground motion amplification in and near Mexico City from strong motion data. *Bull. Seismol. Soc. Am.* 78 (2), 451–477. <https://doi.org/10.1785/BSSA0780020451>.
- Singh, S.K., Quaaas, R., Ordaz, M., Mooser, F., Almora, D., Torres, M., Vásquez, R., 1995. Is there truly a “hard” rock site in the Valley of Mexico? *Geophys. Res. Lett.* 22 (4), 481–484. <https://doi.org/10.1029/94gl03298>.
- Singh, S.K., Cruz-Atienza, V., Pérez-Campos, X., Iglesias, A., Hjörleifsdóttir, V., Reinoso, E., et al., 2018. Deadly intraslab Mexico earthquake of 19 September 2017 (Mw7.1): Ground motion and damage pattern in Mexico City. *Seismol. Res. Lett.* 89 (6). <https://doi.org/10.1785/0220180159>.
- Singh, S.K., Quintanar-Robles, L., Arroyo, D., Cruz-Atienza, V.M., Espíndola, V.H., Bello-Segura, D.L., Ordaz, M., 2020. Lessons from a small local earthquake (Mw3.2) that produced the highest acceleration ever recorded in Mexico City. *Seismol. Res. Lett.* 91 (6). <https://doi.org/10.1785/0220200123>.
- Sirorattanakul, K., Ross, Z.E., Khoshmanesh, M., Cochran, E.S., Acosta, M., Avouac, J.P., 2022. The 2020 Westmorland, California Earthquake Swarm as Aftershocks of a Slow Slip Event Sustained by Fluid Flow. *J. Geophys. Res. Solid Earth* 127 (11). <https://doi.org/10.1029/2022JB024693> e2022JB024693.
- Solano-Rojas, D., Wdowinski, S., Cabral-Cano, E., Osmanoğlu, B., 2020. Detecting differential ground displacements of civil structures in fast-subsiding metropolises with interferometric SAR and band-pass filtering. *Sci. Rep.* 10 (1), 1–14. <https://doi.org/10.1038/s41598-020-72293-z>.
- Srijayanthi, G., Chatterjee, R.S., Kamra, C., Chauhan, M., Chopra, S., Kumar, S., et al., 2022. Seismological and InSAR based investigations to characterise earthquake swarms in Jamnagar, Gujarat, India – An active intraplate region. *J. Asian Earth Sci.* X 8, 100118. <https://doi.org/10.1016/J.JAESX.2022.100118>.
- Suárez, G., Caballero-Jiménez, G.V., Novelo-Casanova, D.A., 2019. Active Crustal Deformation in the Trans-Mexican Volcanic Belt as Evidenced by Historical Earthquakes During the Last 450 Years. *Tectonics* 38 (10), 3544–3562. <https://doi.org/10.1029/2019TC005601>.
- Suárez, G., Ruiz-Barón, D., Chico-Hernández, C., Zúñiga, F.R., 2020. Catalog of Preinstrumental Earthquakes in Central Mexico: Epicentral and Magnitude Estimations Based on Macroseismic Data. *Bull. Seismol. Soc. Am.* 110 (6), 3021–3036. <https://doi.org/10.1785/0120200127>.
- Suter, M., Quintero, O., Johnson, C.A., 1992. Active faults and state of stress in the central part of the Trans-Mexican Volcanic Belt, Mexico I. The Venta de Bravo Fault. *J. Geophys. Res. Solid Earth* 97 (B8), 11983–11993. <https://doi.org/10.1029/91JB00428>.
- Tago, J., Cruz-Atienza, V.M., Villafuerte, C., Nishimura, T., Kostoglodov, V., Real, J., Ito, Y., 2021. Adjoint slip inversion under a constrained optimization framework: Revisiting the 2006 Guerrero slow slip event. *Geophys. J. Int.* 226 (2). <https://doi.org/10.1093/gji/ggab165>.
- Urbina, F., Camacho, C., 1913. La Zona Megasísmica Acambay-Tixmadeje, Estado de México: Conmovida el 19 de Noviembre de 1912. *Boletín Del Instituto Geológico de México*. Imprenta y fototipia de la Secretaría de Fomento.
- Stepinski, T.F., Jasiewicz, J., 2011. Geomorphons-a new approach to classification of landforms. *Proceedings of geomorphometry 2011*, 109–112.
- Vásquez, C. A., Arce, J. L., Rangel, E., Morales-Casique, E., & Arroyo López, S. M. (2021). Arreglo de fracturas geológicas en rocas miocénicas de la cuenca de México. *Revista Mexicana de Ciencias Geológicas*, ISSN-e 2007–2902, ISSN 1026–8774, Vol. 38, No. 1, 2021, Págs. 1–17, 38(1), 1–17. Retrieved from <https://dialnet.unirioja.es/servlet/articulo?codigo=8119108&info=resumen&idioma=SPA>.
- Villafuerte, C., Cruz-Atienza, V.M., Tago, J., Solano-Rojas, D., Garza-Girón, R., Franco, S. I., Dominguez, L.A., Kostoglodov, V., 2025. Slow slip events and megathrust coupling changes contribute to the earthquake potential in Oaxaca, Mexico. *Geophys. J. Inter.* 241 (1), 17–34. <https://doi.org/10.1093/gji/ggaf022>.
- Wang, T.A., Dunham, E.M., 2022. Hindcasting injection-induced aseismic slip and microseismicity at the Cooper Basin Enhanced Geothermal Systems Project. *Sci. Rep.* 12 (1), 1–12. <https://doi.org/10.1038/s41598-022-23812-7>.
- Wen, Y., Xiao, Z., He, P., Zang, J., Liu, Y., Xu, C., 2021. Source Characteristics of the 2020 Mw 7.4 Oaxaca, Mexico, Earthquake Estimated from GPS, InSAR, and Telesismic Waveforms. *Seismol. Res. Lett.* 92 (3), 1900–1912. <https://doi.org/10.1785/0220200313>.
- Wicks, C., Thelen, W., Weaver, C., Gomberg, J., Rohay, A., Bodin, P., 2011. InSAR observations of aseismic slip associated with an earthquake swarm in the Columbia River flood basalts. *J. Geophys. Res. Solid Earth* 116 (B12), 12304. <https://doi.org/10.1029/2011JB008433>.